

Diurnal variation in Mars equatorial odd oxygen species: Chemical production and loss mechanisms



D. Viúdez-Moreiras^{a,b,*}, A. Saiz-Lopez^{b,*}, C.S. Blaszcak-Boxe^c, J.A. Rodriguez Manfredi^a, Y. L. Yung^d

^a Centro de Astrobiología (CSIC-INTA), Spanish National Institute for Aerospace Technology (INTA). Ctra. Ajalvir, km. 4, 28850 Torrejón de Ardoz, Spain

^b Department of Atmospheric Chemistry and Climate, Institute of Physical Chemistry Rocasolano, CSIC. Madrid 28006, Spain

^c Department of Chemistry and Environmental Science, Medgar Evers College-City University of New York, 1650 Bedford Avenue, Brooklyn, NY 11225, USA

^d Division of Geological and Planetary Sciences, California Institute of Technology, Pasadena, CA, USA

ARTICLE INFO

Keywords:

Ozone distribution

Photochemistry

Martian atmosphere modeling

Odd oxygen species

NASA Mars Science Laboratory (MSL)

ABSTRACT

Odd oxygen (O , $O(^1D)$, O_3) abundance and its variability in the Martian atmosphere results from complex physical and chemical interactions among atmospheric species, which are driven mainly by solar radiation and atmospheric conditions. Although our knowledge of Mars' ozone distribution and variability has been significantly improved with the arrival of several recent orbiters, the data acquired by such missions is not enough to properly characterize its diurnal variation. Thus, photochemical models are useful tools to assist in such a characterization. Here, both the Martian ozone vertical distribution and its diurnal variation for equatorial latitudes are studied, using the JPL/Caltech one-dimensional photochemical model and diurnally-variable atmospheric profiles. The chosen equatorial latitude-region is based on the recent and future plans of NASA and other agencies to study this region by different surface missions. A production and loss analysis is performed in order to characterize the chemical mechanisms that drive odd oxygen's diurnal budget and variability on Mars making use of the comprehensive chemistry implemented in the model. The diurnal variation shows large differences in the abundance between daytime and nighttime; and variable behavior depending on the atmospheric layer. The photolysis-driven ozone diurnal profile is obtained at the surface, whilst a sharp decrease is obtained in the upper troposphere at daytime, which originates from the large differences in atomic oxygen abundances between atmospheric layers. Finally, no clear anticorrelation between ozone and water vapor is found in the diurnal cycle, contrary to the strong correlation observed by orbiters on a seasonal timescale.

1. Introduction

The characterization of odd-oxygen (O_x) (O , $O(^1D)$, O_3) is important in Martian atmospheric photochemistry since odd-hydrogen (HO_x) species, produced from water vapor photolysis, compete for atomic oxygen involved in ozone production. HO_x (OH , HO_2 , H) is also involved in the catalytic cycles governing ozone loss (Bates and Nicolet, 1950; Jakosky and Farmer, 1982; Jakosky, 1985; Krasnopolsky, 1993; Nair et al., 1994; Houben et al., 1997; Richardson and Wilson, 2002; Yung and DeMore, 1999; Lefevre et al., 2004; Moudzen and McConnell, 2007). As a result, an anticorrelation between ozone and water vapor profiles appears in Mars' atmosphere (Novak et al., 2002; Fast et al. 2006a; Fast et al., 2006b; Fedorova et al., 2006). These species, with abundances less than 1 part per billion in volume (ppbv), play

fundamental roles in the long-term stability of the CO_2 -dominated atmosphere of Mars and have never been directly measured, with the exception of hydroxyl radical (OH) by Mars Reconnaissance Orbiter (MRO) in recent years at polar regions, and in local winter (Clancy et al., 2013). Therefore, ozone becomes an important tracer for Martian photochemistry and is used for validation of atmospheric models (Lefevre et al., 2004; McElroy and Donahue, 1972; Krasnopolsky, 1993; Nair et al., 1994).

Several orbiters have measured Martian ozone from orbit. NASA's Mariner 7 and Mariner 9 measured ozone column concentrations in the 1970s (Lane et al., 1973; Wehrbein et al., 1979), followed by the Soviet Mars 5 (Krasnopolsky et al., 1975; Krasnopolsky and Parshev, 1979a). In the 1980s Phobos 2 made the first attempts to measure vertical profiles of ozone. The SPICAM instrument onboard Mars Express Orbiter

* Correspondence authors.

E-mail addresses: viudezmd@inta.es (D. Viúdez-Moreiras), a.saiz@csic.es (A. Saiz-Lopez).

<https://doi.org/10.1016/j.icarus.2019.113458>

Received 26 April 2019; Received in revised form 23 September 2019; Accepted 30 September 2019

Available online 15 October 2019

0019-1035/© 2019 The Authors.

Published by Elsevier Inc.

This is an open access article under the CC BY-NC-ND license

(<http://creativecommons.org/licenses/by-nc-nd/4.0/>).

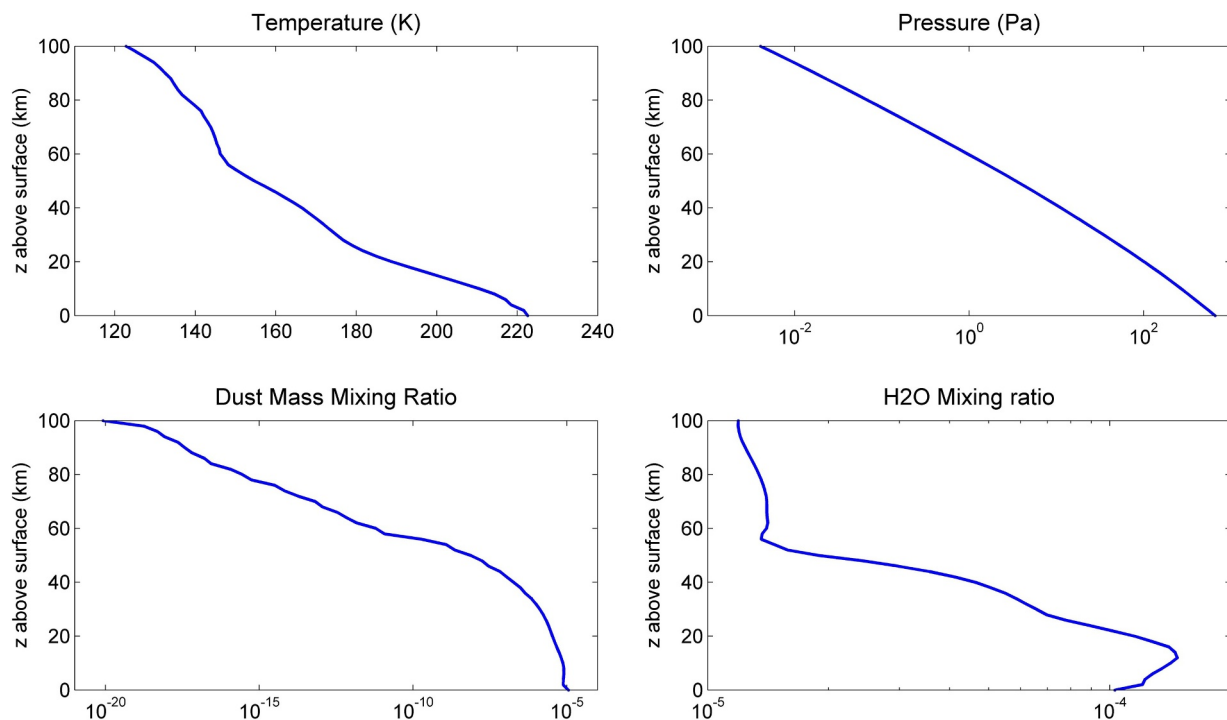


Fig. 1. Vertical profiles under the diurnal-average scenario for the southern fall equinox ($L_s = 0^\circ$) and 4.6° S of latitude, obtained from the MCD (see text).

(Lebonnois et al., 2006; Perrier et al., 2006; Montmessin and Lefevre, 2013; Willame et al., 2017), and NASA's MARCI instrument onboard Mars Reconnaissance Orbiter (MRO) (Clancy et al., 2016) have done extensive measurements of atmospheric ozone. Remote O_3 measurements from Earth have also been performed, both from its surface (Espanak et al., 1991; Fast et al. 2006) and by means of the Hubble Space Telescope (Clancy et al., 1996, 1999).

Martian ozone exhibits high spatial and temporal variability, which makes precise characterization within the atmosphere challenging. Maximum abundances of O_3 can be observed at polar latitudes, where O_3 also shows the greatest seasonal variability: in local winter, the condensation on polar caps removes most of the water vapor from the atmosphere and favors high ozone concentrations with abundances of 30–40 $\mu\text{m-atm}$ (Lefevre et al., 2004; Montmessin and Lefevre, 2013; Clancy et al., 2016; Holmes et al., 2017). The opposite occurs in the local summer when large reservoirs of water ice sublimate, and the resulting high humidity levels cause substantial reductions in atmospheric ozone, even below 1 $\mu\text{m-atm}$ (Lefevre et al., 2004). This process presents asymmetries between both hemispheres due to Mars' sizable eccentricity (0.0934). In addition, there is a strong ozone dependence with latitude and season, where its altitude dependence has been described by measurements (Lebonnois et al., 2006) and photochemical models (Krasnopolsky, 1993; Nair et al., 1994; Yung and DeMore, 1999; Lefevre et al., 2004). Montmessin and Lefevre (2013) reported the existence of an ozone layer that emerges in the southern polar night at 40–60 km in altitude, with no counterpart observed at the North Pole, as a result of the asymmetric large-scale transport of oxygen-rich air from sunlit latitudes to poles. The seasonal variation of the ozone abundance that shapes the annual range is reduced towards moving to equatorial latitudes (Shimazaki and Shimizu, 1979; Lefevre et al., 2004), with ozone column abundance in the range of 0–3 $\mu\text{m-atm}$ for such latitudes (Traub et al., 1979; Barth and Hord, 1971; Barth et al., 1973; Clancy et al., 2016).

Previous model results suggest that ozone abundance also presents a high variability in the diurnal cycle, which is strongly influenced by latitude and season. Different modeling approaches have been used to simulate ozone's temporal distribution on Mars (Krasitskii, 1978;

Shimazaki, 1979; Shimazaki, 1981; Moreau et al., 1991; Nair et al., 1994; Chassefière et al., 1994; Yung and DeMore, 1999; Lefevre et al., 2004; García-Muñoz et al., 2005; Lebonnois, 2006; Krasnopolsky, 2006; Zhu et al., 2007; Holmes et al., 2018) – for example, one/two-dimensional (1D/2D) photochemical models and, more recently, three-dimensional (GCM/3D) models. Each approach has advantages and disadvantages. 1D models have been extensively used in characterizing vertical profiles of species under particular atmospheric assumptions, such as water content or temperature profiles (Yung and DeMore, 1999; Krasnopolsky, 1993; Nair et al., 1994). They are also very useful to manage complex chemistry but without considering advection (horizontal matter/heat transport). In addition, vertical transport is parametrized by means of an eddy diffusion coefficient profile, which does not fully capture the impact of atmospheric transport, such as the coupled interaction between transport and chemistry. First, Krasitskii (1978) studied the globally-averaged diurnal variability in the ozone column using globally-averaged & diurnally-variable estimated atmospheric profiles (i.e. temperature and water mixing ratio) as input conditions. This approach was extended (Nair et al., 1994; Yung and DeMore, 1999; García-Muñoz et al., 2005; Krasnopolsky, 2006) to derive vertical profiles of ozone and other related species under a globally-averaged scenario, but in these cases using constant atmospheric profiles. Shimazaki (1979, 1981) studied the seasonal and diurnal variations, under variable atmospheric profiles, at the subpolar latitude 65°N using a model with 24 reactions and 10 species. Stock et al. (2017) used the JPL/Caltech photochemical model to derive the main reactions and pathways that contribute to the ozone production and loss under a globally and diurnal-average scenario.

On the other hand, General Circulation Models (GCMs), usually without taking into account chemistry (Haberle et al., 1993; Barnes et al., 1993; Shaposhnikov et al., 2016) have been extended to include photochemistry and are now able to simulate such interactions (Lefevre et al., 2004; 2008; Neary and Daerden, 2017; Moudden and McConnell, 2005; González-Galindo et al., 2005; Holmes et al., 2017, 2018) due to advances in High Performance Computing (HPC). As compared to being constrained by an atmospheric vertical column (e.g., 1D models), GCMs model the entire atmosphere. This provides a platform to perform

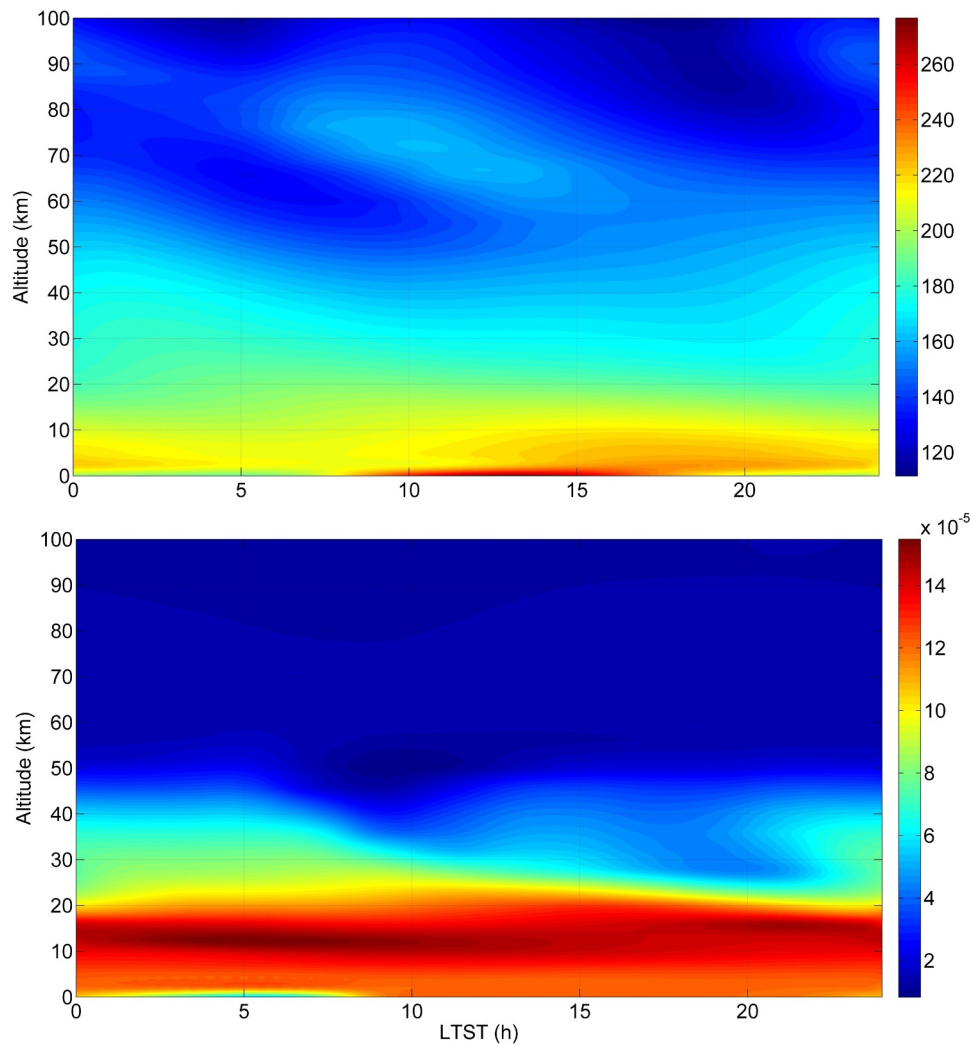


Fig. 2. Diurnal variability of temperature (K) (top) and water volume mixing ratio (bottom) from 0 to 100 km for the southern fall equinox ($L_s = 0^\circ$) and 4.6° S of latitude, obtained from the MCD (see text).

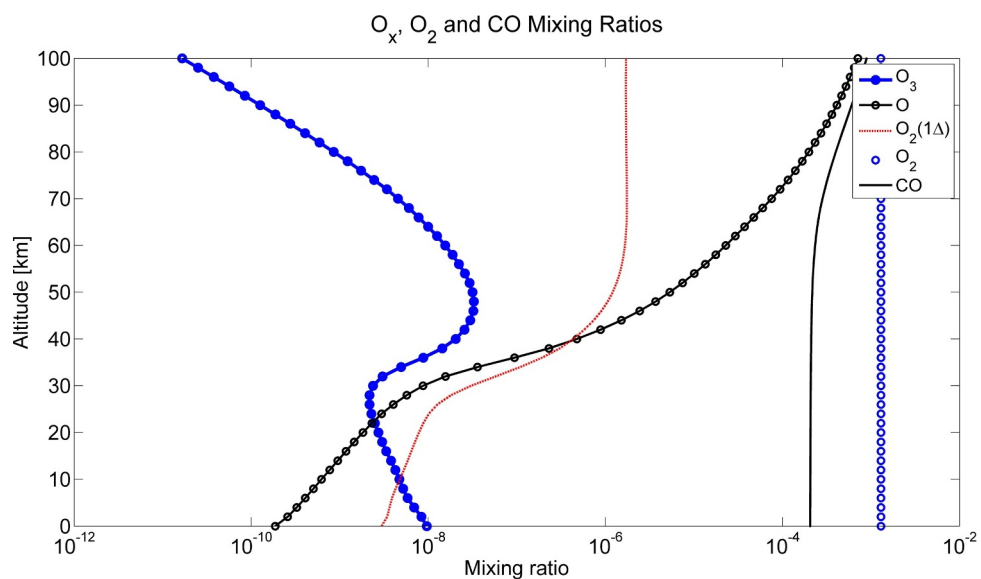


Fig. 3. O_x and CO, O₂ vertical profiles under average conditions, obtained from the JPL/Caltech KINETICS photochemical Mars model.

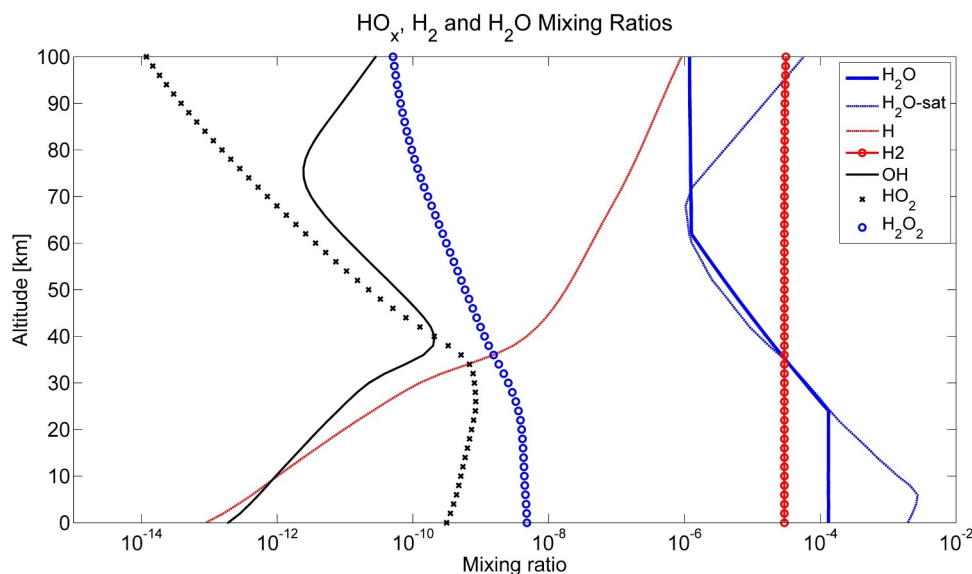


Fig. 4. As Fig. 3 but for HO_x , H_2O_2 , H_2 and H_2O vertical profiles.

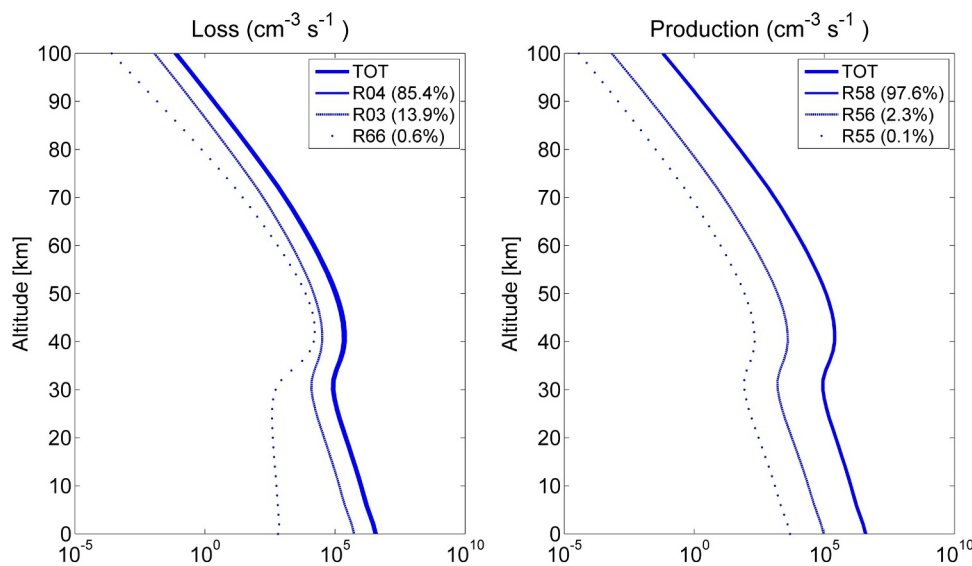


Fig. 5. Vertical profile of ozone production and loss rates under averaged steady state conditions.

simulations that are under scenarios closer to atmospheric conditions – first, by solving approximate-three-dimensional transport equations and by the dynamically coupling water vapor, atmospheric state, and photochemistry. However, due to HPC constraints, they are currently less efficient at managing complex chemistry, and therefore, 1D models become a complementary tool to study the atmosphere. Diurnal and seasonal characterization of the Martian ozone, considering three-dimensional transport was published in Lefevre et al. (2004). Lebonnois et al. (2006) and Perrier et al. (2006) compare these results with ozone profiles derived by SPICAM for different latitudes and seasons, showing in general good agreement with observations, particularly in local winter. Holmes et al. (2018) includes the assimilation of SPICAM observations (Perrier et al., 2006) and models the ozone column abundance as a function of latitude, local time and season.

Here, we perform a detailed diurnal characterization of ozone at equatorial latitudes, focused on the chemical mechanisms that drive its abundance as a function of the local time and atmospheric region. We use the updated version of the JPL/Caltech KINETICS photochemical model of the Martian atmosphere (Nair et al., 1994; Yung and DeMore,

1999; Stock et al., 2012; Boxe et al., 2014), which solves the continuity equations for 28 species and uses a chemical scheme of 151 reactions. Production and Loss (PL) analysis is used to derive the main reactions that contribute to ozone production and loss as a function of the local time and atmospheric region. The latitude-region comes from the recent and future plans of NASA and other agencies to study such a latitude-region by different surface missions. Temperature, pressure and water mixing ratio profiles obtained by the LMD GCM (Forget et al., 1999; Lewis et al., 1999), in accordance to SPICAM data (Forget et al., 2009) onboard Mars Express, and acquired through the Mars Climate Database (MCD), are used to input atmospheric vertical profiles at selected solar longitude and local times in the photochemical model. This represents the first time that a Mars photochemical model with a comprehensive chemistry is forced with diurnal variable atmospheric conditions, and a PL analysis is performed to capture mechanisms that may not be relevant under diurnal-average conditions (Stock et al., 2017), but could play a significant role at particular times within the diurnal cycle.

This paper is structured as follows: Section 2 briefly describes the

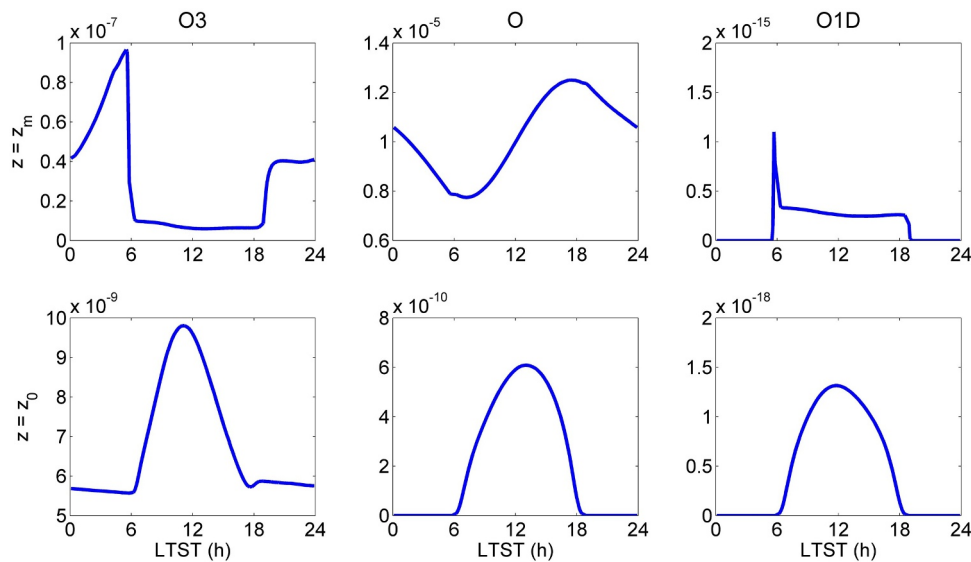


Fig. 6. Diurnal variability of O_3 volume mixing ratio ($L_s = 0^\circ$ and 4.6° S of latitude) at z_0 (2 km of altitude) and z_m (the altitude where the O_3 volume mixing ratio is maximum in diurnal average), obtained from the JPL/Caltech KINETICS photochemical Mars model.

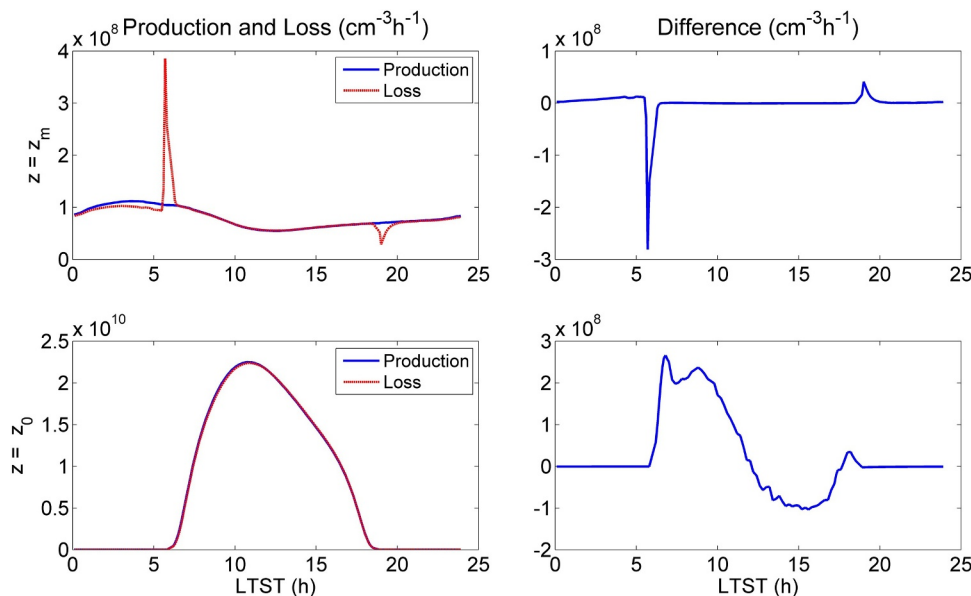


Fig. 7. Comparison between total production and loss rates for ozone ($L_s = 0^\circ$ and 4.6° S) at z_0 and z_m (see text).

JPL/Caltech photochemical model for Mars and presents the temperature, pressure and water vertical profiles input to the model as a function of local time; Section 3 presents and discusses the model results under average conditions, which are used as input for the diurnal time-varying simulations; Section 4 describes the diurnal variability of ozone and other related species, using the aforementioned variable temperature, pressure and water profiles and analyzes the ozone diurnal variability based on by Production and Loss (PL) analysis; and finally, Section 5 presents the conclusions.

2. Derivation of atmospheric conditions and the photochemical model

2.1. Temperature, pressure and water mixing ratio vertical profiles

The variability in atmospheric conditions, such as temperature, pressure and water abundance in the troposphere, plays an important

role on the diurnal variability of the chemical species within the atmosphere. Thus, this work considers variable diurnal atmospheric conditions based on simulated data from the Mars Climate Database (MCD) version 5.3, derived from numerical simulations of the Martian atmosphere generated by the LMD-GCM (Forget et al., 1999; Read et al., 1997; Lewis et al., 1999; Millour et al., 2015). This dataset has been applied to obtain the vertical profiles of pressure, temperature, number density, and water mixing ratio, for the southern fall equinox (L_s $L_s = 0^\circ$) in equatorial latitudes (-4.5° S, 137.4° E), in particular the region where the Mars Science Laboratory (MSL) is located. Here, the standard climatology dust scenario is used, which means a visible optical depth ~ 0.5 at the surface for this region and season.

Fig. 1 shows the resulting vertical profiles adopted for pressure, temperature, dust vertical profile, and water mixing ratio under diurnally-averaged conditions, between 0 and 100 km of altitude. The water saturation profile is also shown, which is a consequence of the adopted vertical temperature profile. Thus, water achieves the

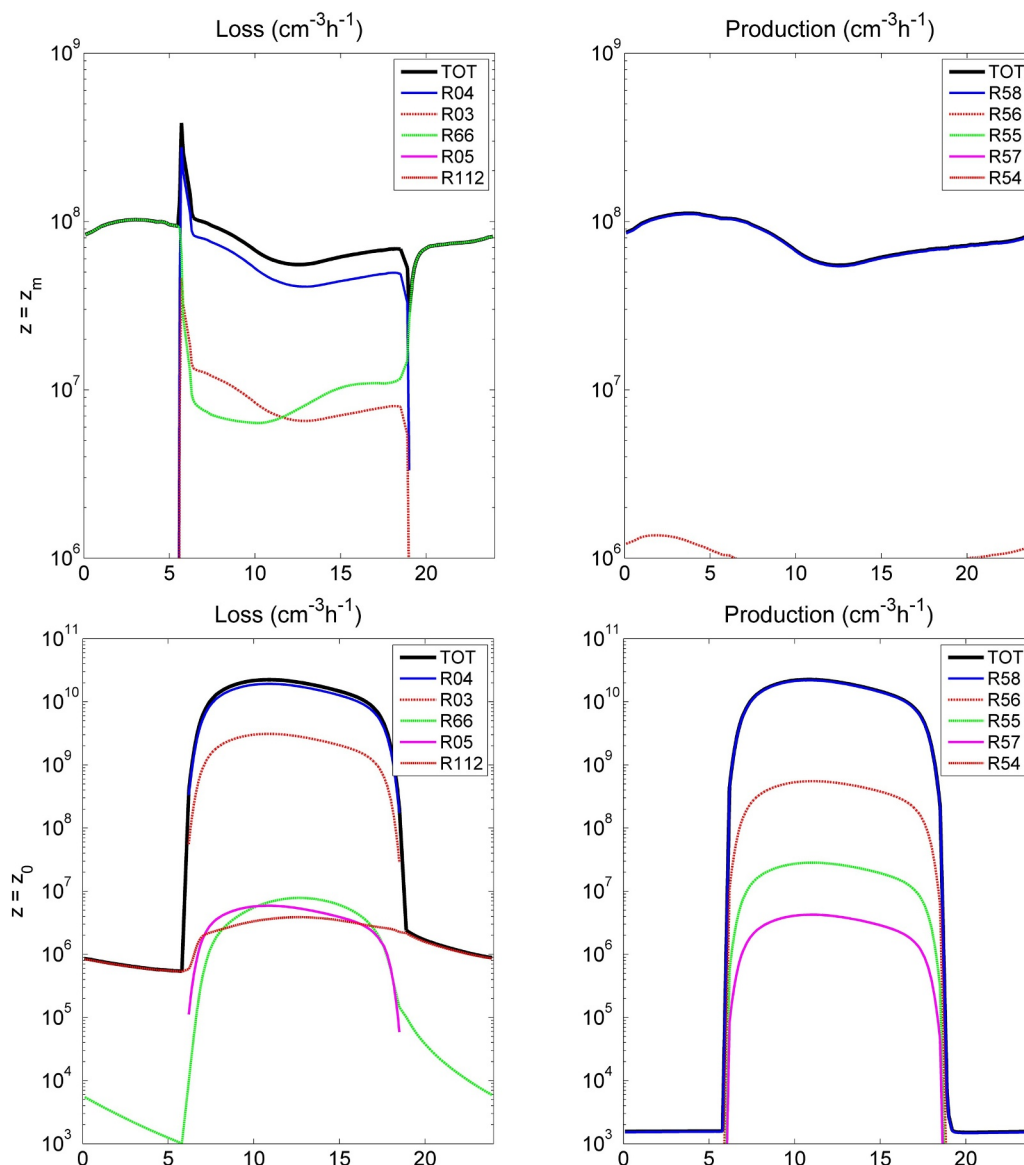


Fig. 8. Ozone production and loss rates variability at two different altitudes. Only the five main contributors for ozone production and loss are shown. Note that photolysis rate lines do not appear during the night due to the logarithmic scale considered in this figure.

saturation level under mean conditions below 30 km, which is in accordance with results obtained e.g. by Steele et al. (2017) and Clancy et al. (2017), and remains supersaturated in accordance to recent measurements, which differs from the idealized vertical profiles (i.e. are not allowed to be supersaturated) usually considered in photochemical models (e.g. Nair et al., 1994; Maltagliati et al., 2011; 2013). The resulting water vapor column abundance of $8.8 \text{ pr-}\mu\text{m}$ under reference conditions is also in accordance to column measurements for this region and season (Smith, 2002; Smith et al., 2009; Toigo et al., 2013).

Fig. 2 shows the diurnal evolution of temperature and water mixing ratio, from 0 to 100 km. Surface temperature shows high diurnal variability (ranging from ~ 200 to 260 K), resulting in maximum values after noon and minima before sunrise. Higher altitudes exhibit several homogenous layers of temperature stratification, where temperature decreases from ~ 220 to $\sim 130 \text{ K}$. Analogously, similar behavior is observed for water mixing ratio, which remains supersaturated in most of the mid to upper troposphere from $\sim 35 \text{ km}$ during nighttime to $\sim 25 \text{ km}$ during daytime.

2.2. JPL/Caltech KINETICS photochemical model

This section briefly describes the JPL/Caltech KINETICS photochemical Mars model. Detailed descriptions can be found in Nair et al. (1994) and Yung and DeMore (1999). The impact of improvements to the chemistry of the Caltech/JPL 1D Mars photochemical model and detailed pathways over mean conditions were described in Boxe et al. (2014) and Stock et al. (2017).

The model solves a set of N coupled one-dimensional continuity equations; where N is the number of species considered in the model with variable abundances over the time domain. Thus, for each instant t of simulation, the model solves, for each species i and at altitude z ,

$$\frac{\partial n_i}{\partial t} + \frac{\partial \phi_i}{\partial z} = P_i - L_i, \quad (1)$$

where n_i is the number density, ϕ_i is the vertical diffuse flux, and P_i and L_i are the production and loss rates, respectively, for a species i . The vertical diffuse flux is computed by

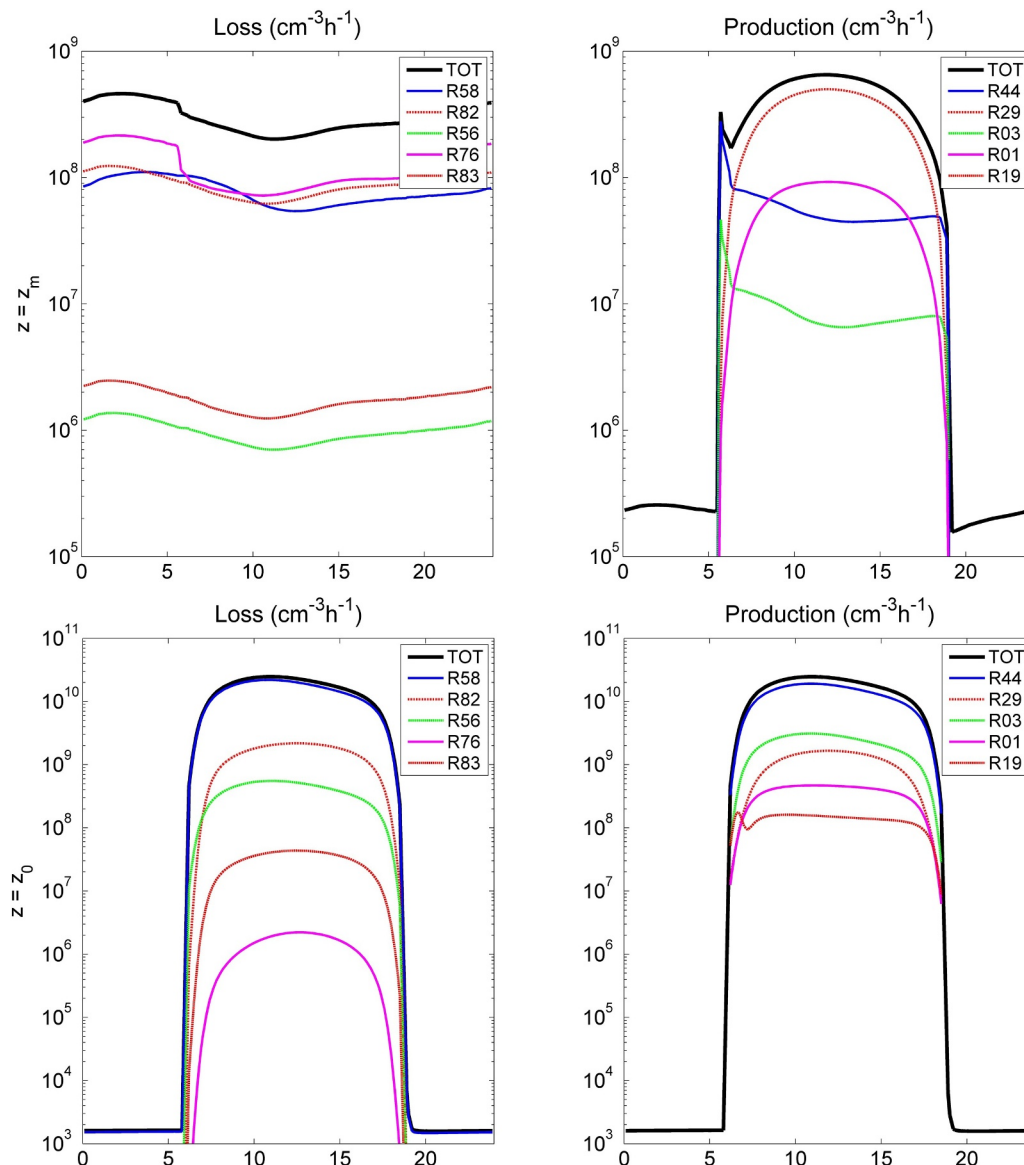


Fig. 9. As Fig. 8 but for atomic oxygen.

$$\phi_i = -D_i \left(\frac{\partial n_i}{\partial z} + \frac{n_i}{H_i} + \frac{n_i(1 + \alpha_i)}{T} \frac{dT}{dz} \right) - K_e \left(\frac{\partial n_i}{\partial z} + \frac{n_i}{H} + \frac{n_i}{T} \frac{dT}{dz} \right), \quad (2)$$

where D_i is the molecular diffusion coefficient of a species i and H_i its scale height, T is the temperature, α_i the thermal diffusion factor, K_e the eddy diffusion coefficient and H the scale height of the atmosphere. The model solves the continuity equations in the current version for $N = 28$ species: O, O(¹D), O₂, O₂(¹Δ), O₃, H, H₂, H₂O, OH, HO₂, H₂O₂, N, N(²D), N₂, NO, NO₂, NO₃, N₂O, N₂O₅, HNO₂, HNO₃, HO₂NO₂, CO, CO₂, O⁺, O₂⁺, CO₂⁺, and CO₂H⁺. The chemical reaction system of the updated model includes 151 reactions, presented in Annex 1, including both the list of reactions along with their kinetics data used in the model. The vertical profile of the eddy diffusion coefficient is taken from Nair et al. (1994).

The vertical grid has a 2 km resolution and is composed of 121 levels reaching 240 km of altitude. The photochemical model includes a coupled radiative transfer model that computes the direct and diffuse components of the radiation field for each vertical level and wavelength in order to compute the photochemical rate constants; this is done by means of a two-stream approximation with multiple scattering, which considers sphericity of the atmosphere. We include dust extinction by means of the vertical profiles generated by the MCD (Fig. 1) with a

visible optical depth ~ 0.5 . Dust single scattering albedo is considered as 0.75 whilst the dust phase function asymmetry parameter is 0.85, which are in accordance with reported values for wavelengths ~ 400 nm (Wolff et al., 2010).

Although some species such as water and hydrogen peroxide are potentially condensable species under Martian atmospheric conditions, the outputs from the MCD consider a slight supersaturation of water in the middle atmosphere, which is in accordance with recent observations and differs from the idealized vertical profiles usually considered in photochemical models (Maltagliati et al., 2011, 2013) and in previous analysis using this model (Nair et al., 1994; Boxe et al., 2014; Stock et al., 2017). The detailed input water vertical profiles to the JPL/Caltech photochemical model are presented in Sections 3 and 4.

Mixing ratios vertical profiles are initialized from a diurnal average, and are performed, with updated atmospheric conditions (Section 2.1) as a function of the local time each 20 min along the simulation time, using a timestep of 30 s, until reaching a steady state diurnal variation.

The lower boundary conditions are mixing ratios of 0.027 for N₂, 0.953 for CO₂, and zero for ions, in accordance to Nair et al. (1994) and Franz et al. (2015). Upper boundary conditions are H and H₂ effusion velocities of 3.1×10^3 and 34 cm/s, respectively. The model is also

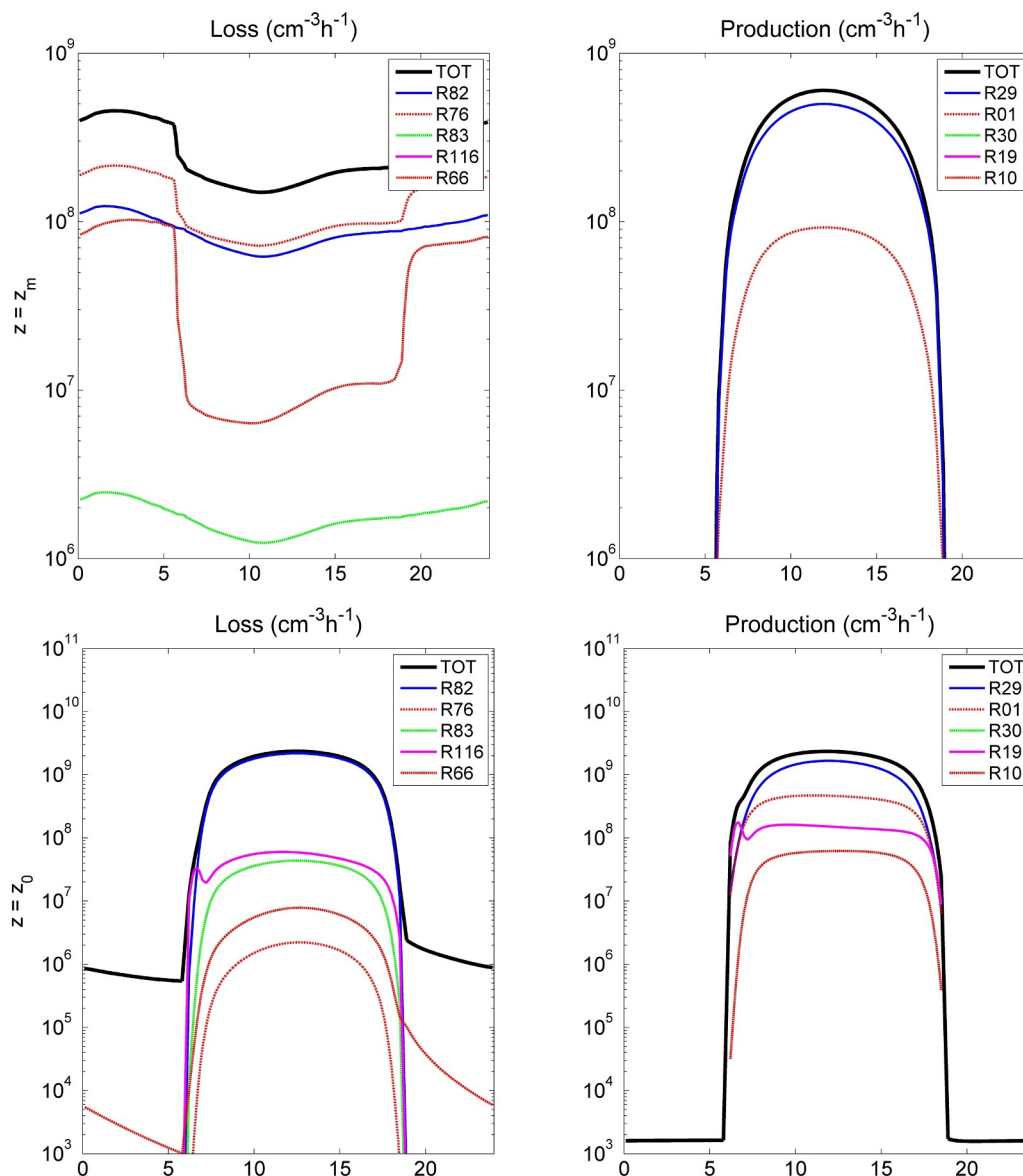


Fig. 10. As Fig. 8 but for Ox species.

constrained by an escape flux of atomic oxygen at the upper boundary of $1.2 \times 10^8 \text{ cm}^2/\text{s}$. Zero fluxes were assumed for all other species as upper and lower boundary conditions (see e.g. Nair et al., 1994 and Yung and DeMoore, 1999 for more details).

3. Photochemical simulations under average conditions

The updated version of the JPL/Caltech KINETICS photochemical Mars model was installed at the CSIC computers, and simulations were performed for average conditions; on the one hand, to validate the photochemical model with previous results; and on the other hand, to use the results in the mixing ratio vertical profiles, for the chemical species involved in the model, as initial conditions for the diurnal cycle scenario (Section 4).

Fig. 3 shows the O_x , O_2 and CO vertical profiles up to an altitude of 100 km, which show similar profiles to those presented in Boxe et al. (2014) and Stock et al. (2017). Note that those simulations were performed without the presence of dust. Here, slight differences in species abundances are present mainly as a result of radiation that reaches the

lower levels of the atmosphere. Surface mixing ratio of oxygen ($\sim 1.4 \times 10^{-3}$) is in agreement with empirical data (Hartogh et al., 2010; Trainer et al., 2014; Franz et al., 2015). However, although CO mixing ratio (1.9×10^{-4}) is next to the lower limit of the reported observational range (2.0×10^{-4} – 1.3×10^{-3}) measured by CRISM (Smith et al., 2009), the lower limit of CO concerns the summer polar regions when CO_2 sublimation leads to a seasonal decrease in the mixing ratio of non-condensable species; therefore, the globally-averaged value is expected to be higher, which is a well-known trouble in photochemical models. This could result from uncertainties in the rate constants, cross sections, atmospheric vertical profiles used, and/or the lack of a more complex chemical scheme involving heterogeneous chemistry (Nair et al., 1994; Anbar et al., 1993; Atreya and Gu, 1994; Lefevre et al., 2008; Krasnopolsky and Lefevre, 2013).

The model predicts two ozone peaks, one in the lower troposphere (LT) and the other in the upper troposphere (UT), which is in agreement with previous model results (Nair et al., 1994; Lefevre et al., 2004; Krasnopolsky, 2006). The transition between these layers can be established from a chemical perspective as the altitude in which the

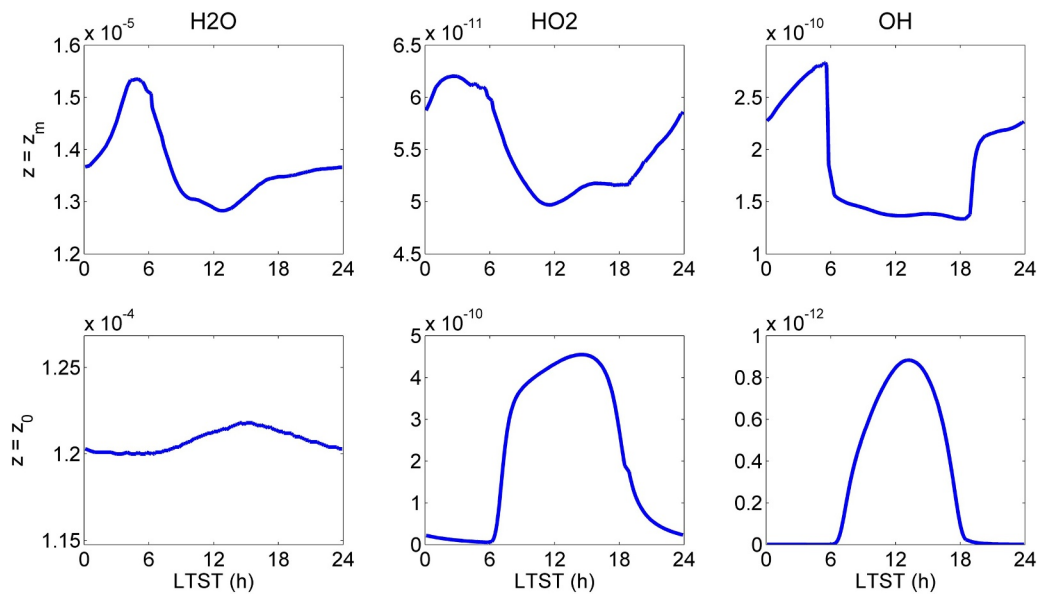


Fig. 11. As Fig. 6, but for HOx volume mixing ratio.

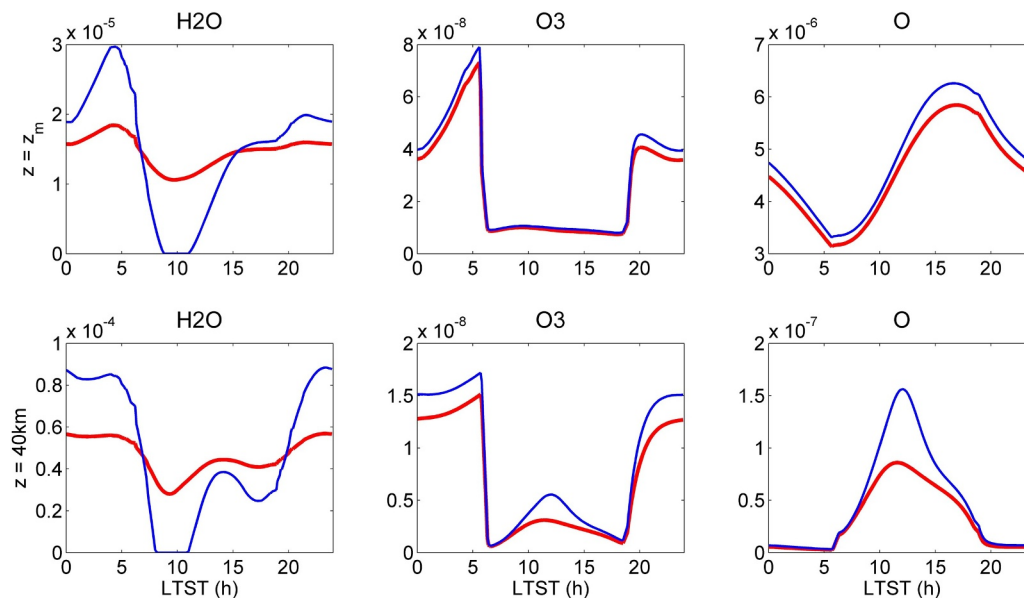


Fig. 12. Effect of increasing the amplitude of the diurnal variation in water vapor by a factor of 5 on the ozone and atomic oxygen mixing ratios, for ~ 54 km (top) and 40 km of altitude (bottom). Red lines show the *nominal* case and blue lines the simulated case under enhanced diurnal variation in water vapor. (For interpretation of the references to color in this figure legend, the reader is referred to the web version of this article.)

ozone mixing ratio (X_{O_3}) and atomic oxygen mixing ratio (X_O) profiles intersect (Fig. 1 in Stock et al., 2017). Thus, the ozone abundance in the LT region, where $X_O < X_{O_3}$ is directly controlled by the reservoir species CO_2 and O_2 by means of their photolyses. However, as atomic oxygen quickly increases with altitude, exceeding the ozone abundance in the UT region $X_O > X_{O_3}$ it directly drives the ozone abundance. The minimum between both ozone peaks (z_r) is placed roughly at 30 km for averaged conditions. The highest ozone mixing ratio, around 10^{-7} , is modelled in the UT, at an altitude, z_m , ~ 50 km, while the maximum mixing ratio in the lower troposphere is located at surface levels, with a mixing ratio of $\sim 10^{-8}$. Hence, the model predicts an average ozone column abundance of $0.6 \mu\text{m-atm}$, which is within the range of reported orbital measurements, $0\text{--}3 \mu\text{m-atm}$ (Lane et al., 1973; Wehrbein et al., 1979; Perrier et al., 2006; Clancy et al., 2016). The simulated $O_2(^1\Delta)$ mean vertical profile corresponds with ~ 1.5 MR, in agreement with

column observations from Mars' orbit (Fedorova et al., 2006), ground-based observations and model (Krasnopolsky, 2013).

Fig. 4 shows the OH, HO_2 , H_2 and H_2O vertical profiles under mean conditions; the water vapor mixing ratio is shown, in addition to its saturation profile. As described, this averaged profile, corresponding to an $8.8 \text{ pr-}\mu\text{m}$ column abundance of water vapor, remains constant in the simulation up to mesospheric altitudes in which water is undersaturated and where its mixing ratio is computed consistently with the other species (Nair et al., 1994). OH mixing ratio profile presents a peak at ~ 40 km of altitude. H_2O_2 mean mixing ratio (ratio of H_2O_2 column abundance to the total column abundance) is ~ 4.3 ppbv, in agreement with classical photochemical models and below recent observations $\sim 10\text{--}30$ ppbv (e.g. Moudden, 2007; Krasnopolsky, 2009; Encrenaz et al., 2012; 2015), suggesting a production mechanism not contemplated in the current chemical scheme.

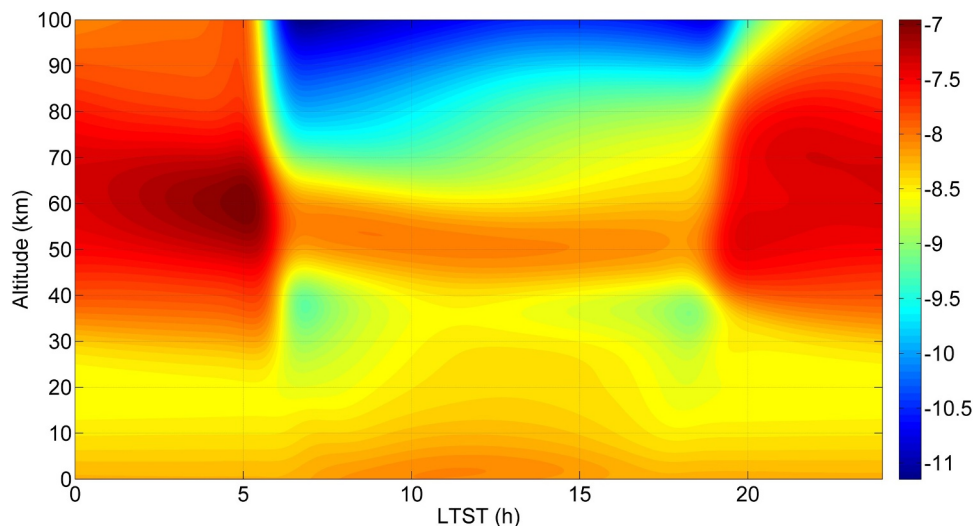


Fig. 13. Diurnal variability for the vertical profile of ozone at the southern fall equinox. The logarithm of ozone mixing ratio is plotted.

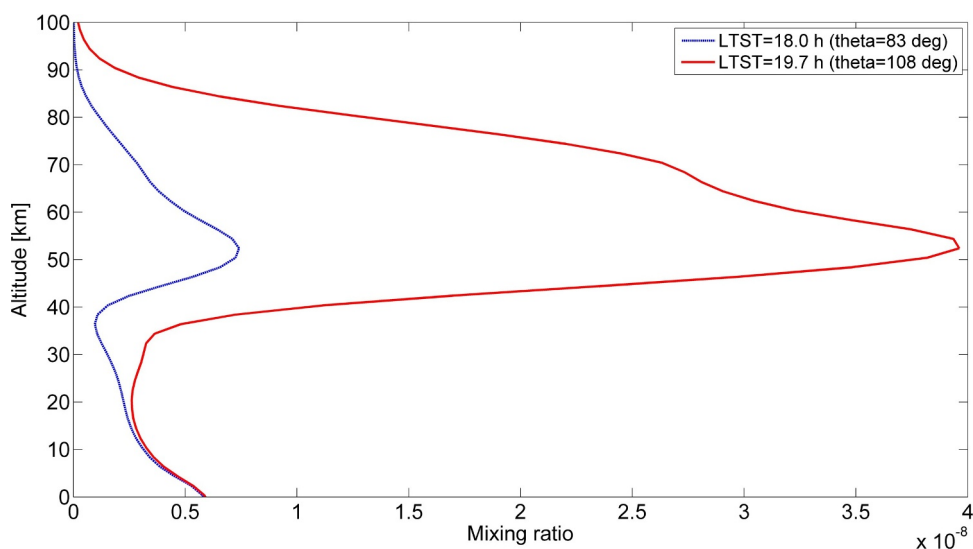


Fig. 14. Comparison between vertical profiles of ozone mixing ratio at sunset (18:00 LT and \sim 19:40 LT).

The ozone production and loss rates (Fig. 5) are approximately $10^7 \text{ cm}^{-3} \text{ s}^{-1}$ at the surface. Ozone is produced by the termolecular reaction between atomic and molecular oxygen in presence of a third body (Annex 1:chemical scheme), mainly CO_2 or N_2 (R58 and R56), representing 97.6% and 2.3%, respectively, of the total ozone production under mean conditions. The loss is dominated by ozone photolysis, producing molecular and atomic oxygen; both excited (R4) and in ground state (R3) contributing \sim 85% and \sim 14%, respectively, to the total ozone loss. The ozone production and loss rates are increased in the UT region, which exhibits quite active ozone photochemistry. However, a significant amount of ozone is recycled through null cycles. Detailed pathways for ozone production and loss, derived for a globally-averaged steady state scenario, were previously identified in Stock et al. (2017) by means of Pathway Analysis Program (PAP) (Lehmann, 2004). Their analysis under a globally-averaged steady state scenario resulted in quite different ozone production and loss pathways contribution depending on the altitude region.

Table A.2 (left column) shows the main pathways for ozone production (LT_P1, LT_P2 and LT_P3) and loss (LT_L1) in the LT region. CO_2 and O_2 photodissociation are the most important contributors to the atomic oxygen production. In addition, NO_2 photolysis, enhanced by

catalytic HO_x cycles, also contributes to ozone production, where the most relevant precursor of atomic oxygen in the Martian atmosphere is the photolysis of CO_2 . Under mean atmospheric conditions, the CO_2 photolysis pathway represents the most important contribution to the O_3 production rate (\sim 60%) (Stock et al., 2017), while the O_2 photodissociation pathway represents \sim 20%. The NO_2 precursor contributes \sim 15% while the remaining production percentage is attributed to minor catalytic pathways. O_3 photolysis represents the largest loss of this species and results in the production of excited and ground state O and O_2 , respectively, whereas catalytic HO_x processes compete for the atomic oxygen generated as a product of O_3 photolysis.

Table A.2 (right column) shows the main pathways for ozone production (UT_P1) and loss (UT_L1 to UT_L3) in the UT region. As atomic oxygen abundance in the UT region is greater than the ozone abundance, the production of the atomic oxygen by CO_2 , O_2 and NO_2 photolyses does not control the O_3 production in this region. Here, ozone production is directly dominated by the termolecular reaction UT_P1, which directly depends on oxygen abundance. This behavior differs from the LT region. In addition, PAP analysis, under a globally-averaged steady state scenario, suggests that vertical transport also plays a strong contribution (Stock et al., 2017). PAP analysis also shows that the net

ozone loss is mainly driven by ozone photolysis (UT_L1), as in the lower troposphere, but the direct loss involving HO_x species is also evident in this region (UT_L2 and UT_L3). Therefore, the variability in the atomic oxygen number density profile determines the characteristic ozone profile in UT since atomic oxygen dominates and strongly increases with altitude (Fig. 4). The total number density follows an opposite trend, resulting in the characteristic rate and vertical abundance profiles, with an ozone local maximum in the upper troposphere.

4. Results and discussion

4.1. Odd oxygen diurnal variability and production and loss analysis

The previous section showed the model results under average conditions. In reality, the atmosphere is not in steady-state, but different processes, such as the variable solar irradiation during the daytime, produce disturbances on the abundance of atmospheric species. In addition, atmospheric conditions and chemical composition exhibit strong latitudinal and longitudinal variability. Although these effects can be neglected in a first term for some species, such as CO₂ (its chemical lifetime is much greater than 1 year), the chemical lifetime of odd oxygen species such as ozone is of order of a few hours or even lower (Nair et al., 1994), suggesting a diurnal cycle.

Thus, simulations constrained with atmospheric conditions from MCD / LMD GCM output data (see Section 2), can give new insights into the atmospheric chemistry involved in a particular environment, taking advantage of the comprehensive chemistry implemented in our 1D photochemical model. Therefore, simulations are performed with updated atmospheric conditions as a function of the local time each 20 min along the simulation time (see Section 2), using a diurnal-average scenario as initial conditions. This section presents the diurnal cycle of O₃ and other trace gas species (O, O(¹D), H₂O, HO₂, OH) at the southern fall equinox, for an equatorial latitude of 4.5° south (the Gale crater, the landing site of the MSL), and analyzes such a variability by means of PL analysis. Note that the resolution of the MCD grid is larger than Gale crater, and therefore the crater is not resolved.

Ozone shows different diurnal behavior at different altitudes due to the variable contribution of the chemical pathways in the LT and UT, as described in the previous Section, and the different abundance of the species involved in the ozone production and loss. Fig. 6 shows the variability in the O_x mixing ratio (O₃, O, O(¹D)) for two different altitudes: i) z₀ (2 km of altitude) and, ii) the altitude where the O₃ mixing ratio is maximum in diurnal average (z_m) (54 km of altitude). The reason for presenting the z₀ altitude level instead of 0 km is to minimize possible effects due to boundary conditions of the model. Also, note that the z_m value, obtained from averaging the maximum in the vertical profile of O₃ mixing ratio among the diurnal variable simulations, slightly differs from the value reached in the diurnal average simulation (50 km of altitude). This is due to: (i) the fact that initial conditions, generated from a global model perspective, and then input as initial conditions to the simulations in the southern latitude constrained with atmospheric profiles for this particular location; (ii) the diurnal average radiation field used in the diurnal-average simulation does not fully represent the resulting diurnal average O₃ abundance due to non-linearities in the model (Stock et al., 2017).

It can be seen that the near-surface ozone presents a sharp increase in its mixing ratio during sunrise, reaching a peak at 10 AM (SZA ~ 40°). After this time, a sharp decrease is observed, stabilizing after sunset (SZA ~ 110°). The mixing ratio is then roughly constant until the sunrise, which suggests that ozone behaves as a quasi-passive species during nighttime, when photolysis is inhibited.

The ozone diurnal variability changes completely in the UT region, illustrated by the plot for altitude z_m showed in Fig. 6. There, ozone shows a sharp decrease during sunrise due to photolysis (5 AM, SZA ~ 110°) that reduces its abundance by a factor of 7. It remains roughly constant until sunset (at these altitudes) (7 PM, SZA ~ 110°). When

sunlight disappears the ozone mixing ratio abruptly increases, reaching steady state until 12 PM. The UT ozone presents higher abundances during the nighttime, in contrast to what it is modeled for surface ozone, and in general for LT ozone. The difference in LT and UT atomic oxygen abundances (~10⁻¹⁰ vs. ~10⁻⁵) can explain this behavior.

Fig. 7 shows the ozone production and loss rates and their difference, for the aforementioned altitudes, and Fig. 8 splits the production and loss rates into their major contributors. As displayed in Fig. 7, O₃ is most of time at photochemical equilibrium between PL processes. Departures from this photochemical equilibrium are however visible during sunrise and sunset at z_m and also during the day at the LT region.

Thus, ozone concentration is fairly constant during the nighttime at z₀. Here, the production is dominated by the termolecular reaction between atomic and molecular oxygen in presence of CO₂ as a third body (R58). In addition, N₂ and O₂ also contribute as a third body both in the LT and UT region by means of R56 and R55, respectively, although to a lesser extent, in accordance to their abundances and reaction kinetics. The loss in the LT region is dominated by the reaction with NO, R112; and with atomic hydrogen, R66, in the UT region. The production and loss rates at night in the LT layer are negligible, and therefore, their difference does not significantly change ozone's abundance. The atmosphere is, however, more reactive in the UT region during nighttime, and R58 compensates the loss, dominated by R66. This is another example of the altitude dependence in the contribution of different chemical pathways. As temperatures are colder overnight, reaction kinetics in R58 and R66 tend to increase the ozone abundance (Fig. 6).

At sunrise, ozone is quickly photolyzed in the UT by R4 and R3, producing O(¹D) and O respectively, where O(¹D) is quickly deactivated by R44. However, ozone production remains roughly constant at sunrise by R58 and cannot compensate for this sharp increase in ozone photolysis and the fact that no other reaction significantly modifies the large amount of atomic oxygen present in the UT region. As a result, ozone abundance quickly decreases along with the R66, R4 and R3 rates. Then, production and loss are roughly stabilized during daytime until sunset. Then, ozone photolysis stops leading to an ozone abundance rise due to R58 as well as an increase in R66 rate until it equals the total ozone production rate, which will be maintained until sunrise.

However, the additional source of atomic oxygen in the LT region (Fig. 6) from CO₂, O₂ and NO₂ photolysis implies a net production that increases the ozone abundance until 10:00 LTST (Local True Solar Time), when it inverts this trend due to the decrease in atomic oxygen until sunset. Both production and loss are stabilized after sunset, when photolysis ceases and the loss is dominated by the reaction with NO (R112).

The abrupt increase and subsequent decrease in the excited atomic oxygen in the UT region, during sunrise, is driven by ozone photolysis (involved in UT_L1). Therefore, as ozone decays after sunrise, the mixing ratio of excited atomic oxygen evolves accordingly. The scenario is quite different in the LT region, where the scattered sunlight at sunrise makes a gradual increase in the O₃ photolysis rates when compared to those observed in the UT region (R4, R3, and even R5, the last one negligible in the UT region).

As described, the atomic oxygen increases during daytime in the UT (Fig. 6), as a result of the photolysis of different species (Fig. 9), such as CO₂ (R29, involved in LT_P1), O₂ (R1, involved in LT_P2) and NO₂ (R19, involved in LT_P3). O₃ is not a net contributor to atomic oxygen, since it not only participates in its production (R4 and R3) but also contributes to its loss (R58, R56, R55). Here, the large amount of atomic oxygen resulting in the UT region prevents strong diurnal changes as seen in LT. Despite that, the difference between the O production and loss is evident in the UT.

During daytime, the increase in R58, but also in R82 and R76, involving OH and HO₂ respectively, cannot compensate for the increase in O production by the aforementioned photolysis reactions, and the O concentration increases (Fig. 8). The opposite occurs at night, when atomic oxygen production is negligible and when the rate of the reaction

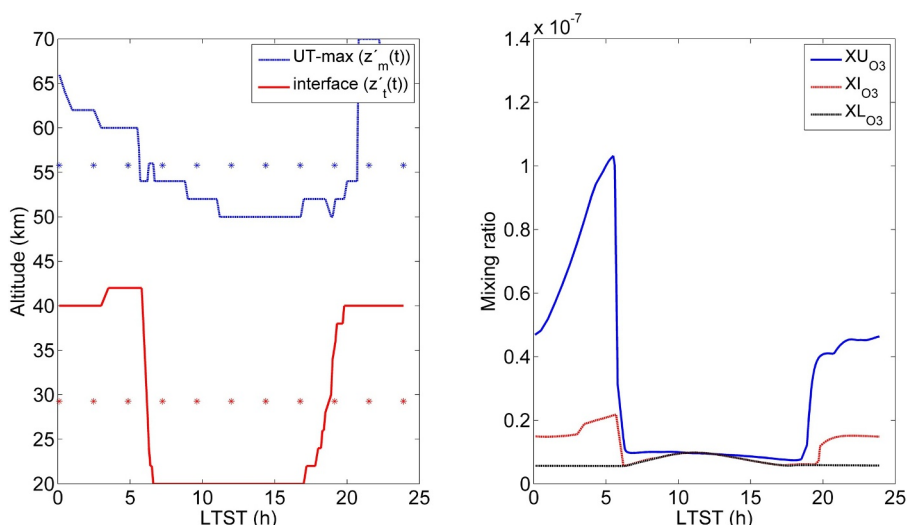


Fig. 15. left: diurnal evolution for the altitude transition between ozone layers ($z'_t(t)$) and at the maximum upper tropospheric values in the mixing ratio profiles ($z'_m(t)$). Their diurnal averages (z_t and z_m respectively) are also shown in dot lines. Right: diurnal variability in ozone mixing ratios at z_m (XU_{O_3}), z_t (XI_{O_3}) and for the near-surface ozone (XL_{O_3}).

with OH (R76) increases, with a consequent decrease in nocturnal O.

In fact, the catalytic cycles involving HO_x species lead to a loss of O_x (O + O(¹D) + O₃), not O₃ alone. For instance, Figs. 9 and 10 show that the most important O_x loss process in the LT is R82, since the other reactions shown are fast reactions of exchange within the O_x family. Fig. 11 shows the PL results obtained for the O_x family species. The fast reactions between O_x members are removed and, therefore, the *net* contributors are easily identified by means of this approach. Both LT and UT regions show that the main contributor to the O_x production is the CO₂, O₂ and NO₂ photolysis (R29, R01 and R19 respectively), in accordance to the main pathways derived by PAP analysis for O₃ under diurnal-average conditions (Stock et al., 2017; Table A.2). The main O_x loss mechanisms differ from the UT and LT. Thus, the LT is clearly dominated by the reaction between atomic oxygen and HO₂ (R82). However, the reaction between atomic oxygen and OH dominates in the UT region due to the differences in HO_x family abundances. In addition, the direct loss of O₃ by R66 plays a significant role in the O_x loss in the UT, particularly at night.

Thus, HO_x species are strongly involved in catalytic O₃ and O_x family production and loss pathways in both regions. Fig. 11 shows the variability in the HO₂ and OH mixing ratios, and their driver, H₂O, for the same altitudes presented in Fig. 6. At the LT region, H₂O evolves according to the surface temperature, increasing its abundance during daytime.

As a consequence, the HO₂ and OH diurnal variabilities, which appear to be directly linked to the solar irradiation, are shaped by the H₂O evolution, moving the peak values to the afternoon. The evolution is quite different in the UT region. Here, water mixing ratio remains supersaturated during the day, with roughly constant values (Fig. 2). The HO₂ mixing ratio decreases between sunrise and 10:00 LTST, when it starts to increase. The OH mixing ratio shows a similar trend to that observed for ozone due to the relationship between ozone loss and hydroxyl radical production (R66), with maxima mixing ratios at night. These results suggest there is no clear anticorrelation between H₂O and O₃ from a diurnal timescale, which is reported in the literature for a seasonal timescale (Novak et al., 2002; Fast et al. 2006a; Fast et al., 2006b). This result is due to the fact that the diurnal variation of water in the simulations is not enough to induce such an anticorrelation observed in a seasonal timescale. We have repeated the simulations performed under the *nominal* diurnal scenario, but considering an enhanced diurnal amplitude of water vapor in the atmosphere by a factor of 5. Fig. 12 shows the results in both scenarios. The high variation of H₂O

abundance in the diurnal cycle does not produce a significant variation in O₃, even in the *enhanced* scenario. This is because the strong reduction in HO_x production via H₂O photolysis during the daytime, peaking at ~10:00 LTST, has a little effect on atomic oxygen abundance, given its high abundance at the ~ z_m level. It is therefore necessary to look at lower altitudes (e.g. 40 km, Fig. 12), where atomic oxygen abundances are orders of magnitude lower (Fig. 3), to appreciate significant effects in O₃ from the H₂O abundance variation, within the diurnal timescale.

4.2. Ozone vertical profiles

Figs. 13 and 14 show the ozone vertical profile as a function of LTST. The vertical profile follows a similar pattern to those presented in Section 4 for mean conditions, in accordance to Nair et al. (1994) and Yung and DeMore (1999), but the absolute mixing ratios varies with time. The sharp change in ozone mixing ratio is also seen in Fig. 14 for the particular case of the sunset. Here, ozone ranges from 7×10^{-9} at 18:00 in the UT layer 3.5×10^{-8} , 1.5 h later. Also, the relative abundance between the UT and LT layers (illustrated by the local maxima at z_m and z_0) varies with time. $z'_m(t)$ remains roughly constant during the daytime around 55 km, increasing to 65–70 km during the nighttime. This altitude depends on the temperature and water mixing ratio profiles, and thus a seasonal variation as a function of the temperature and water mixing ratio profiles is expected. Closer published empirical profiles taken at night next to the southern fall equinox and equatorial latitudes, shown in Lebonnois et al. (2006), are in agreement with our simulated profiles.

This evolution can be seen in more detail in Fig. 15. The plot on the right shows the maximum mixing ratio values as a function of LTST, for the LT region (XL_{O_3}), the UT region (XU_{O_3}), and the interface region (XI_{O_3}), taken at z_m , z_0 and z_t , respectively. The left hand plot shows the altitude in which the ozone mixing ratio and the atomic oxygen mixing ratio profiles intersect (whose diurnal average is z_t , also showed in dotted line), in addition to the altitude for the maximum upper tropospheric ozone mixing ratio (whose diurnal average is z_m , also showed in dotted line). The LT ozone peaks at the surface. Therefore, model results suggest that these characteristic levels of the ozone profile strongly vary between daytime and nighttime, ranging from 20 km during daytime to 42 km during nighttime for z_t , and 50 km to 65–70 km for z_m .

Ozone in the LT region increases its chemical lifetime from less than an hour during daytime to more than a year at night, suggesting the ozone loss is completely controlled by its photolysis. Note that ozone

deposition is not included in the model. This strong increase in lifetime is not observed in the UT region, where ozone increases its lifetime but always below one hour, due to the different chemical mechanisms involved in the destruction processes between both regions (see Fig. 8).

Note that, in addition to systematic measurement errors in empirical data and modeling deviations, the vertical profiles adopted here could have biases with the representative vertical profiles for average and diurnal conditions, which would result in biases in the resulting species abundances. Furthermore, this approach does not consider horizontal transport. Uncertainties in the kinetic rate constants and/or the lack of a more complex chemistry involving other species and reactions, and heterogeneous chemistry (Nair et al., 1994; Lefevre, 2008; Anbar et al., 1993; Atreya and Gu, 1994; Lefevre et al., 2008) could be a source of biases in the ozone and other vertical profiles. A detailed study concerning the effect of uncertainties in the species abundances and variability will contribute new valuable data to this characterization. Nevertheless, our modeled ozone abundance results are in good agreement with orbital measurements (Krasnopolsky et al., 1975; Krasnopolsky and Parshev, 1979a; Perrier et al., 2006; Clancy et al., 2016), suggesting that the one dimensional photochemical model with atmospheric vertical profiles assimilation is able to reproduce the observational data for the particular season and latitudes presented in this study.

5. Summary and conclusions

This study has presented a diurnal characterization of O_x ($O + O(^1D) + O_3$) for an equatorial latitude, based on the JPL/Caltech KINETICS one-dimensional photochemical model, in a nominal dust scenario for an illustrative fall equinox. This represents the first time that a Mars photochemical model with a comprehensive chemistry is forced with diurnal variable atmospheric conditions, and a PL analysis is performed in order to capture mechanisms that may not be relevant under diurnal-average conditions, but could play a significant role at particular times within the diurnal cycle, and therefore drive the species abundances.

Input atmospheric conditions, including pressure, temperature and water vertical profiles, are obtained from the MCD, generated by GCM output data in accordance to SPICAM from Mars Express. Species modeled concentrations are in agreement with their available empirical data. Here, the water vertical profile reaches supersaturation in accordance to recent measurements in most of the mid to upper troposphere from ~ 35 km during nighttime to ~ 25 km during daytime. It differs from the idealized vertical profiles usually utilized in photochemical models, which consider that water is saturated in the Martian atmosphere, which implies more water vapor is allowed in the atmosphere in average, impacting the ozone abundance due to catalytic loss pathways involving HO_x species.

Model results suggest a pronounced diurnal variability in the ozone abundance between daytime and nighttime, and different behavior depending on the atmospheric layer. A solar-driven ozone diurnal profile is obtained at the surface, whilst a sharp decrease is obtained in the daytime upper troposphere, which comes from the large differences in atomic oxygen abundances between these regions. The comprehensive chemical scheme implemented in the KINETICS model allows for investigating this behavior by means of the Production and Loss (PL) analysis, identifying the principal reactions that contribute to ozone production and loss, as a function of local time and atmospheric layer.

The catalytic cycles involving HO_x species are also investigated. In fact, the catalytic cycles involving HO_x species lead to a loss of O_x , not O_3 alone. The main O_x loss mechanisms are different as a function of atmospheric layer. For instance, the lower troposphere is clearly dominated by the reaction between atomic oxygen and HO_2 . However, the reaction between atomic oxygen and OH dominates in the upper troposphere due to the differences in the HO_x family abundances. In addition, the direct loss of O_3 by the reaction with atomic hydrogen plays a key role in the O_x loss in the upper troposphere, particularly at night. No clear anticorrelation between ozone and water vapor is found

in the diurnal cycle, contrary to the strong correlation observed by orbiters in a seasonal timescale, suggesting the amount of water variation in the atmosphere is not enough to lead such an anticorrelation observed in a seasonal timescale.

Annex 1: Chemical Scheme

Both model input and outputs presented here are available in the Supplementary Material. The MCD data used here is also available through the MCD LMD website.

Table A.1

Set of chemical reactions with their chemical rate constants.

	Reaction	Rate constant
R1	$O_2 + h\nu \rightarrow 2O$	
R2	$O_2 + h\nu \rightarrow O + O(^1D)$	
R3	$O_3 + h\nu \rightarrow O_2 + O$	
R4	$O_3 + h\nu \rightarrow O_2(^1\Delta) + O(^1D)$	
R5	$O_3 + h\nu \rightarrow O_2 + O(^1D)$	
R6	$O_3 + h\nu \rightarrow O_2(^1\Delta) + O$	
R7	$O_3 + h\nu \rightarrow 3O$	
R8	$H_2 + h\nu \rightarrow 2H$	
R9	$OH + h\nu \rightarrow O + H$	
R10	$HO_2 + h\nu \rightarrow OH + O$	
R11	$H_2O + h\nu \rightarrow H + OH$	
R12	$H_2O + h\nu \rightarrow H_2 + O(^1D)$	
R13	$H_2O + h\nu \rightarrow 2H + O$	
R14	$H_2O_2 + h\nu \rightarrow 2OH$	
R15	$N_2 + h\nu \rightarrow N + N(^2D)$	
R16	$N_2 + h\nu \rightarrow 2N$	
R17	$N_2 + h\nu \rightarrow 2N(^2D)$	
R18	$NO + h\nu \rightarrow N + O$	
R19	$NO_2 + h\nu \rightarrow NO + O$	
R20	$NO_3 + h\nu \rightarrow NO_2 + O$	
R21	$NO_3 + h\nu \rightarrow NO + O_2$	
R22	$N_2O + h\nu \rightarrow N_2 + O(^1D)$	
R23	$N_2O_5 + h\nu \rightarrow NO_2 + NO_3$	
R24	$N_2O_5 + h\nu \rightarrow NO + NO_3 + O$	
R25	$HNO_2 + h\nu \rightarrow OH + NO$	
R26	$HNO_3 + h\nu \rightarrow NO_2 + OH$	
R27	$HO_2NO_2 + h\nu \rightarrow HO_2 + NO_2$	
R28	$HO_2NO_2 + h\nu \rightarrow OH + NO_3$	
R29	$CO_2 + h\nu \rightarrow CO + O$	
R30	$CO_2 + h\nu \rightarrow CO + O(^1D)$	
R31	$O + M + h\nu \rightarrow O^+ + e^- + M$	
R32	$O_2 + h\nu \rightarrow O_2^+ + e^-$	
R33	$CO_2 + h\nu \rightarrow CO_2^+ + e^-$	
R34	$CO_2 + h\nu \rightarrow CO + O^+ + e^-$	
R35	$O_2^+ + e^- \rightarrow 2O$	$6.60E-05 T^{-1}$
R36	$CO_2^+ + e^- \rightarrow CO + O$	$3.80E-07$
R37	$CO_2H^+ + e^- \rightarrow CO_2 + H$	$3.00E-07$
R38	$O^+ + CO_2 \rightarrow O_2^+ + CO$	$9.60E-10$
R42	$O(^1D) + O_2 \rightarrow O + O_2$	$3.20E-11 e^{(70/T)}$
R43	$O(^1D) + N_2 \rightarrow O + N_2$	$1.80E-11 e^{(110/T)}$
R44	$O(^1D) + CO_2 \rightarrow O + CO_2$	$7.40E-11 e^{(120/T)}$
R45	$O(^1D) \rightarrow O + h\nu$	$6.70E-03$
R46	$O_2(^1\Delta) + O \rightarrow O_2 + O$	$2.00E-16$
R47	$O_2(^1\Delta) + O_2 \rightarrow 2O_2$	$3.60E-18 e^{(-220/T)}$
R48	$O_2(^1\Delta) + H_2O \rightarrow O_2 + H_2O$	$4.80E-18$
R49	$O_2(^1\Delta) + N_2 \rightarrow O_2 + N_2$	$1.00E-20$
R50	$O_2(^1\Delta) + CO \rightarrow O_2 + CO$	$1.00E-20$
R51	$O_2(^1\Delta) + CO_2 \rightarrow O_2 + CO_2$	$2.00E-20$
R52	$O_2(^1\Delta) \rightarrow O_2 + h\nu$	$2.58E-04$
R53	$2O + M \rightarrow O_2 + M$	$k_0 = 5.21E-35 e^{(900/T)}$
R54	$2O + O_2 \rightarrow O_3 + O$	$k_0 = 5.90E-34 (T/300)^{-2.4}$ $k_\infty = 2.80E-12$
R55	$O + 2O_2 \rightarrow O_3 + O_2$	$k_0 = 5.90E-34 (T/300)^{-2.4}$ $k_\infty = 2.80E-12$
R56	$O + O_2 + N_2 \rightarrow O_3 + N_2$	$k_0 = 5.95E-34 (T/300)^{-2.3}$
R57	$O + O_2 + CO \rightarrow O_3 + CO$	$k_0 = 6.70E-34 (T/300)^{-2.5}$ $k_\infty = 2.80E-12$
R58	$O + O_2 + CO_2 \rightarrow O_3 + CO_2$	$k_0 = 5.00E-35 e^{(724/T)}$
R59	$O + O_2 + M \rightarrow O_3 + M$	$k_0 = 6.00E-34 (T/300)^{-2.4}$
R60	$H + O_2 + M \rightarrow HO_2 + M$	

(continued on next page)

Table A.1 (continued)

	Reaction	Rate constant
		$k_0 = 5.70E-32 (T/300)^{-1.6}$
		$k_{\infty} = 7.50E-11 (T/300)$
R61	$N + O_2 \rightarrow NO + O$	$1.50E-11 e^{(-3600/T)}$
R62	$O + O_3 \rightarrow 2O_2$	$8.00E-12 e^{(-2060/T)}$
R63	$O(^1D) + O_3 \rightarrow 2O_2$	$1.20E-10$
R64	$O(^1D) + O_3 \rightarrow 2O + O_2$	$1.20E-10$
R65	$O_2(^1\Delta) + O_3 \rightarrow 2O_2 + O$	$5.20E-11 e^{(-2840/T)}$
R66	$H + O_3 \rightarrow OH + O_2$	$1.40E-10 e^{(-470/T)}$
R67	$OH + O_3 \rightarrow HO_2 + O_2$	$1.70E-12 e^{(-940/T)}$
R68	$OH + O_3 \rightarrow HO_2 + O_2(^1\Delta)$	$3.20E-14 e^{(-940/T)}$
R69	$HO_2 + O_3 \rightarrow OH + 2O_2$	$1.00E-14 e^{(-490/T)}$
R70	$N + O_3 \rightarrow NO + O_2$	$2.00E-16$
R71	$O + H + M \rightarrow OH + M$	$k_0 = 1.30E-29 (T)^{-1.0}$
R72	$2H + M \rightarrow H_2 + M$	$k_0 = 2.70E-31 (T)^{-0.6}$
R73	$O + H_2 \rightarrow OH + H$	$8.50E-20 T^{2.7} e^{(-3160/T)}$
R74	$O(^1D) + H_2 \rightarrow H + OH$	$1.10E-10$
R75	$OH + H_2 \rightarrow H_2O + H$	$5.50E-12 e^{(-2000/T)}$
R76	$O + OH \rightarrow O_2 + H$	$2.20E-11 e^{(120/T)}$
R77	$H + OH + N_2 \rightarrow H_2O + N_2$	$k_0 = 6.10E-26 (T)^{-2.0}$
R78	$H + OH + CO_2 \rightarrow H_2O + CO_2$	$k_0 = 7.70E-26 (T)^{-2.0}$
R79	$2OH \rightarrow H_2O + O$	$4.20E-12 e^{(-240/T)}$
R80	$N + OH \rightarrow NO + H$	$3.80E-11 e^{(85/T)}$
R81	$2OH + M \rightarrow H_2O_2 + M$	$k_0 = 6.20E-31 (T/300)^{-1.0}$ $k_{\infty} = 2.60E-11 (T/300)$
R82	$O + HO_2 \rightarrow OH + O_2$	$3.00E-11 e^{(200/T)}$
R83	$O + HO_2 \rightarrow OH + O_2(^1\Delta)$	$6.00E-13 e^{(200/T)}$
R84	$H + HO_2 \rightarrow 2OH$	$7.21E-11$
R85	$H + HO_2 \rightarrow H_2 + O_2$	$7.29E-12$
R86	$H + HO_2 \rightarrow H_2 + O_2(^1\Delta)$	$1.30E-13$
R87	$H + HO_2 \rightarrow H_2O + O$	$1.62E-12$
R88	$OH + HO_2 \rightarrow H_2O + O_2$	$4.80E-11 e^{(250/T)}$
R89	$OH + HO_2 \rightarrow H_2O + O_2(^1\Delta)$	$9.60E-13 e^{(250/T)}$
R90	$2HO_2 \rightarrow H_2O_2 + O_2$	$2.30E-13 e^{(600/T)}$
R91	$2HO_2 \rightarrow H_2O_2 + O_2(^1\Delta)$	$4.60E-15 e^{(600/T)}$
R92	$2HO_2 + M \rightarrow H_2O_2 + O_2 + M$	$k_0 = 1.70E-33 e^{(1000/T)}$
R93	$O(^1D) + H_2O \rightarrow 2OH$	$2.20E-10$
R94	$O + H_2O_2 \rightarrow OH + HO_2$	$1.40E-12 e^{(-2000/T)}$
R95	$OH + H_2O_2 \rightarrow H_2O + HO_2$	$2.90E-12 e^{(-160/T)}$
R96	$O_2(^1\Delta) + N \rightarrow NO + O$	$9.00E-17$
R97	$N(^2D) + O \rightarrow N + O$	$6.90E-13$
R98	$N(^2D) + N_2 \rightarrow N + N_2$	$1.70E-14$
R99	$N(^2D) + NO \rightarrow N_2 + O$	$6.90E-11$
R100	$N(^2D) + CO \rightarrow N + CO$	$1.70E-12$
R101	$N(^2D) + CO_2 \rightarrow NO + CO$	$3.50E-13$
R102	$N(^2D) \rightarrow N + hv$	$1.07E-05$
R103	$N + HO_2 \rightarrow NO + OH$	$2.20E-11$
R104	$N_2O_5 + H_2O \rightarrow 2HNO_3$	$2.00E-21$
R105	$2N + M \rightarrow N_2 + M$	$k_0 = 8.27E-34 e^{(490/T)}$
R106	$O(^1D) + N_2 + M \rightarrow N_2O + M$	$k_0 = 3.50E-37 (T/300)^{-0.6}$
R111	$O + NO + M \rightarrow NO_2 + M$	$k_0 = 9.00E-31 (T/300)^{-1.5}$ $k_{\infty} = 3.00E-11 (T/300)$
R112	$O_3 + NO \rightarrow NO_2 + O_2$	$3.00E-12 e^{(-1500/T)}$
R113	$OH + NO + M \rightarrow HNO_2 + M$	$k_0 = 7.00E-31 (T/300)^{-2.6}$ $k_{\infty} = 3.60E-11 (T/300)^{-0.1}$
R114	$HO_2 + NO \rightarrow NO_2 + OH$	$1.12E-12 e^{(250/T)}$
R115	$N + NO \rightarrow N_2 + O$	$2.10E-11 e^{(100/T)}$
R116	$O + NO_2 \rightarrow NO + O_2$	$5.60E-12 e^{(180/T)}$
R117	$O + NO_2 + M \rightarrow NO_3 + M$	$k_0 = 2.50E-31 (T/300)^{-1.8}$ $k_{\infty} = 2.20E-11 (T/300)^{-0.7}$
R118	$O_3 + NO_2 \rightarrow NO_3 + O_2$	$1.20E-13 e^{(-2450/T)}$
R119	$H + NO_2 \rightarrow OH + NO$	$4.00E-10 e^{(-340/T)}$
R120	$OH + NO_2 + M \rightarrow HNO_3 + M$	$k_0 = 2.00E-30 (T/300)^{-3.0}$ $k_{\infty} = 2.50E-11 (T)$
R121	$HO_2 + NO_2 \rightarrow HNO_3 + O_2$	$5.00E-16$
R122	$HO_2 + NO_2 + M \rightarrow HO_2NO_2 + M$	$k_0 = 1.80E-31 (T/300)^{-3.2}$ $k_{\infty} = 4.70E-11 (T/300)^{-1.4}$
R123	$N + NO_2 \rightarrow N_2O + O$	$5.80E-12 e^{(220/T)}$
R124	$NO_3 + NO_2 \rightarrow NO + NO_2 + O_2$	$4.50E-14 e^{(-1260/T)}$
R125	$NO_3 + NO_2 + M \rightarrow N_2O_5 + M$	$k_0 = 2.00E-30 (T/300)^{-4.4}$ $k_{\infty} = 1.40E-12 (T/300)^{-0.7}$
R126	$O + NO_3 \rightarrow O_2 + NO_2$	$1.00E-11$
R127	$H + NO_3 \rightarrow OH + NO_2$	$1.10E-10$
R128	$OH + NO_3 \rightarrow HO_2 + NO_2$	$2.20E-11$
R129	$HO_2 + NO_3 \rightarrow HNO_3 + O_2$	$3.50E-12$
R130	$NO + NO_3 \rightarrow 2NO_2$	$1.50E-11 e^{(170/T)}$
R131	$2NO_3 \rightarrow 2NO_2 + O_2$	$8.50E-13 e^{(-2450/T)}$

Table A.1 (continued)

	Reaction	Rate constant
R132	$CO + NO_3 \rightarrow NO_2 + CO_2$	$4.00E-19$
R133	$O(^1D) + N_2O \rightarrow 2NO$	$6.70E-11$
R134	$O(^1D) + N_2O \rightarrow N_2 + O_2$	$4.90E-11$
R135	$O + N_2O_5 \rightarrow 2NO_2 + O_2$	$3.00E-16$
R136	$N_2O_5 + M \rightarrow NO_3 + NO_2 + M$	$6.00E-04 T^{-4.4} e^{(-10990/T)}$
R137	$O_3 + HNO_2 \rightarrow O_2 + HNO_3$	$5.00E-19$
R138	$OH + HNO_2 \rightarrow H_2O + NO_2$	$1.80E-11 e^{(-390/T)}$
R139	$O + HNO_3 \rightarrow OH + NO_3$	$3.00E-17$
R140	$OH + HNO_3 \rightarrow NO_3 + H_2O$	$7.20E-15 e^{(785/T)}$
R141	$O + HO_2NO_2 \rightarrow OH + NO_2 + O_2$	$7.80E-11 e^{(-3400/T)}$
R142	$OH + HO_2NO_2 \rightarrow H_2O + NO_2 + O_2$	$1.30E-12 e^{(380/T)}$
R143	$HO_2NO_2 + M \rightarrow HO_2 + NO_2 + M$	$8.57E-05 T^{-3.2} e^{(-10900/T)}$
R144	$O + CO + M \rightarrow CO_2 + M$	$k_0 = 1.70E-33 e^{(-1510/T)}$ $k_{\infty} = 2.66E-14 e^{(-1459/T)}$
R145	$O + 2CO \rightarrow CO_2 + CO$	$k_0 = 6.50E-33 e^{(-2180/T)}$
R146	$2O + CO \rightarrow CO_2 + O$	$k_0 = 3.40E-33 e^{(-2180/T)}$
R147	$OH + CO \rightarrow CO_2 + H$	$1.50E-13$
R148	$CO_2 + O \rightarrow O_2 + CO$	$1.64E-10$
R149	$CO_2 + O \rightarrow O^+ + CO_2$	$9.62E-11$
R150	$CO_2 + H_2 \rightarrow CO_2H^+ + H$	$4.70E-10$
R167	$HO_2 + NO \rightarrow HNO_3$	$9.14E-31 e^{(1644/T)}$

Table A.2

Ozone production and loss pathways in LT region (left) and UT region (right) taken from Stock et al. (2017)

	LT_P1	UT_P1
	$CO_2 + hv \rightarrow CO + O$	
	$O + O_2 + M \rightarrow O_3 + M$	
net:	$O_2 + CO_2 \rightarrow O_3 + CO$	
	LT_P2	
	$O_2 + hv \rightarrow 2O$	
	$2(O + O_2 + M \rightarrow O_3 + M)$	
net:	$3O_2 \rightarrow 2O_3$	
	LT_P3	UT_P1
	$OH + CO \rightarrow CO_2 + H$	$O + O_2 + M \rightarrow O_3 + M$
	$H + O_2 + M \rightarrow HO_2 + M$	
	$HO_2 + NO \rightarrow NO_2 + OH$	
	$NO_2 + hv \rightarrow NO + O$	UT_L1
	$O + O_2 + M \rightarrow O_3 + M$	$O_3 + hv \rightarrow O_2 + O$
net:	$2O_2 + CO \rightarrow O_3 + CO_2$	UT_L2
		$H + O_3 \rightarrow OH + O_2$
		$O + OH \rightarrow O_2 + H$
		$O_3 + O \rightarrow 2O_2$
	LT_L1	UT_L3
	$O_3 + hv \rightarrow O_2 + O$	$H + O_3 \rightarrow OH + O_2$
	$O + HO_2 \rightarrow O_2 + OH$	$CO + OH \rightarrow CO_2 + H$
	$OH + CO \rightarrow CO_2 + H$	
	$H + O_2 + M \rightarrow HO_2 + M$	
net:	$O_3 + CO \rightarrow O_2 + CO_2$	net:
		$O_3 + CO \rightarrow O_2 + CO_2$

Declaration of Competing interest

The authors declare no conflict of interest.

Acknowledgments

This research has been supported by the Spanish Ministry of Economy and Competitiveness(MINECO), under projects ESP2014-54256-C4-1-R and ESP2016-79612-C3-1-R. The authors thank Michael D. Smith and an anonymous reviewer, whose comments helped improve this paper.

Supplementary materials

Supplementary material associated with this article can be found, in the online version, at [doi:10.1016/j.icarus.2019.113458](https://doi.org/10.1016/j.icarus.2019.113458).

References

- Anbar, A.D., Leu, M.-T., Nair, H.A., Yung, Y.L., 1993. Adsorption of HOx on aerosol surfaces: implications for the atmosphere of Mars. *J. Geophys. Res.* 98, 10933–10940.
- Atreya, S.K., Gu, Z.G., 1994. Stability of the Martian atmosphere: is heterogeneous catalysis essential. *J. Geophys. Res.* 99, 13133–13145.

- Barnes, J.R., Pollack, J.B., Haberle, R.M., Leovy, C.B., Zurek, R.W., Lee, H., Schaeffer, J., 1993. Mars atmospheric dynamics as simulated by the NASA Ames general circulation model: II. Transient baroclinic eddies. *J. Geophys. Res.* 98 (E2), 3125–3148.
- Barth, C.A., Hord, C.W., 1971. Mariner ultraviolet spectrometer: topography and polar cap. *Science* 173, 197–201.
- Barth, C.A., Hord, C.W., Stewart, A.I., Lane, A.L., Disk, M.L., Anderson, G.P., 1973. Mariner 9 ultraviolet spectrometer experiment: seasonal variations of ozone on Mars. *Science* 179, 795–796.
- Bates, D.R., Nicolet, M., 1950. The photochemistry of atmospheric water vapour. *J. Geophys. Res.* 55, 301–327.
- Boxe, C.S., Francisco, J.S., Shia, R.-L., Yung, Y.L., Nair, H., Liang, M.C., Saiz-Lopez, A., 2014. New insights into Martian atmospheric chemistry. *Icarus* 242, 97–104.
- Chassefière, E., Rosenqvist, J., Théodore, B., 1994. Ozone as a tracer of turbulence induced by breaking gravity waves on Mars. *Planet. Space Sci.* 42 (10), 825–830. ISSN 0032-0633.
- Clancy, R.T., Wolff, M.J., James, P.B., Smith, E., Billawala, Y.N., Lee, S.W., Callan, M., 1996. Mars ozone measurements near the 1995 aphelion: hubble space telescope ultraviolet spectroscopy with the faint object spectrograph. *J. Geophys. Res.* 101 (E5), 12777–12783. <https://doi.org/10.1029/96JE00835>.
- Clancy, R.T., Wolff, M.J., James, P.B., 1999. Minimal aerosol loading and global increases in atmospheric ozone during the 1996–1997 Martian northern spring season. *Icarus* 138, 49–63.
- Clancy, R.T., Wolff, M.J., Lefevre, F., Cantor, B.A., Malin, M.C., Smith, M.D., 2016. Daily global mapping of Mars ozone column abundances with MARCI UV band imaging. *Icarus* 266, 112–133.
- Clancy, R.T., Sandor, B.J., García-Muñoz, A., Lefevre, F., Smith, M.D., Wolff, M.J., Montmessin, F., Murchie, S., Nair, H., 2013. First detection of Mars atmospheric hydroxyl: CRISM Near-IR measurement versus LMD GCM simulation of OH Meinel band emission in the Mars polar winter atmosphere. *Icarus* 226, 272–281.
- Clancy, R.T., Smith, M., Lefevre, F., McConnochie, T.H., Sandor, B., Wolff, M., Lee, S.W., Murchie, S.L., Toigo, A.D., Nair, H., Navarro, T., 2017. Vertical profiles of Mars 1.27 μm O₂ dayglow from MRO CRISM limb spectra: seasonal/global behaviors, comparisons to LMDGCM simulations, and a global definition for Mars water vapor profiles. *Icarus* 293, 132–156, 2017.
- Daerden, F., Neary, L., Clancy, R.T., Smith, M., 2017. Improved GEM-Mars GCM with atmospheric chemistry. In: 6th International Workshop on the Mars Atmosphere: Modeling and Observations. Granada, 2017.
- Encrenaz, T., Greathouse, T.K., Lefevre, F., et al., 2012. *Plan. Space Sci.* 68, 3.
- Encrenaz, T., et al., 2015. Seasonal variations of hydrogen peroxide and water vapor on Mars: further indications of heterogeneous chemistry. *A&A* 578, A127.
- Espenak, F., Mumma, M.J., Kostiuik, T., Zipoy, D., 1991. Ground-based infrared measurements of the global distribution of ozone in the atmosphere of Mars. *Icarus* 92, 252–262.
- Fast, K., et al., 2006. Ozone abundance on Mars from infrared heterodyne spectra I. Acquisition, retrieval, and anticorrelation with water vapor. *Icarus* 181, 491–431.
- Fast, K., et al., 2006. Ozone abundance on Mars from infrared heterodyne spectra II. Validating photochemical models. *Icarus* 183, 396–402.
- Fedorova, A., Korabiev, O., Bertaux, J.L., Rodin, A., Kiselev, A., Perrier, S., 2006. Mars water vapor abundance from SPICAM IR spectrometer: seasonal and geographic distributions. *J. Geophys. Res.* 111 (9).
- Forget, F., Hourdin, F., Fournier, R., Hourdin, C., Talagrand, O., Collins, M., Lewis, S.R., Read, P.L., Huot, J.-P., 1999. Improved general circulation models of the Martian atmosphere from the surface to above 80 km. *J. Geophys. Res.* 104 (E10), 24155–24175. <https://doi.org/10.1029/1999JE001025>.
- Forget, F., Montmessin, F., Bertaux, J.L., Gonzalez-Galindo, F., Lebonnois, S., Quemerais, E., Reberac, A., Dimarellis, E., López Valverde, M.A., 2009. Density and temperatures of the upper Martian atmosphere measured by stellar occultations with Mars Express SPICAM. *J. Geophys. Res.* 114, E01004.
- Franz, H.B., et al., 2015. Reevaluated Martian atmospheric mixing Ratios from the mass spectrometer on the curiosity rover. *Planet. Space Sci.* 109–110, 154–158.
- García-Muñoz, A., McConnell, J.C., McDade, I.C., Melo, S.M.L., 2005. Airglow on Mars: some model expectations for the OH Meinel bands and the O₂ IR atmospheric band. *Icarus* 176 (1), 75–95.
- González-Galindo, F., López-Valverde, M.A., Angelats i Coll, M., Forget, F., 2005. Extension of a Martian general circulation model to thermospheric altitudes: UV heating and photochemical models. *J. Geophys. Res.* 110, E09008. <https://doi.org/10.1029/2004JE002312>.
- Haberle, R.M., et al., 1993. Mars atmospheric dynamics as simulated by the NASA Ames General Circulation Model, I. The zonal-mean circulation. *J. Geophys. Res.* 98, 3093–3123.
- Hartogh, P., et al., 2010. Herschel/HIFI observations of Mars: first detection of O₂ at submillimetre wavelengths and upper limits on HCl and H₂O₂. *A&A* 521, L49.
- Holmes, J.A., Lewis, S.R., Patel, M.R., 2017. On the link between martian total ozone and potential vorticity. *Icarus* 282, 104–117.
- Holmes, J.A., Lewis, S.R., Patel, M.R., Lefevre, F., 2018. A reanalysis of ozone on Mars from assimilation of SPICAM observations. *Icarus* 302, 308–318.
- Houben, H., Haberle, R.M., Young, R.E., Zent, A.P., 1997. Modeling the Martian seasonal water cycle. *J. Geophys. Res.* 102, 9069–9084.
- Jakosky, B.M., 1985. The seasonal cycle of water on Mars. *Space Sci. Rev.* 41, 131–200.
- Jakosky, B.M., Farmer, C.B., 1982. The seasonal and global behavior of water vapor in the Mars atmosphere – complete global results of the Viking atmospheric water detector experiment. *J. Geophys. Res.* 87, 2999–3019.
- Krasitskii, O.P., 1978. A model for the diurnal variation of the composition of the Martian atmosphere (*Kosmicheskie Issledovaniia*, 16, May–June 1978, 434–442.). *Cosm. Res.* 16 (3), 350–356. Nov. 1978Translation.
- Krasnopolsky, V.A., Krysko, A.A., Rogachev, V.N., 1975. Measurement of ozone in a planetary atmosphere by space probe Mars-5. *Kosmicheskie Issledovaniia* 13, 37–41 (translation: *Cosmic Research*, 13, 31–34).
- Krasnopolsky, V.A., Parshev, V.A., 1979. Ozone and photochemistry of the Martian lower atmosphere. *Planet. Space Sci.* 27, 113–120.
- Krasnopolsky, V.A., 1993. Photochemistry of the Martian atmosphere (mean conditions). *Icarus* 101, 313–332.
- Krasnopolsky, V.A., 2006. Photochemistry of the Martian atmosphere: seasonal, latitudinal, and diurnal variations. *Icarus* 185 (1), 153–170. ISSN 0019-1035.
- Krasnopolsky, V.A., 2009. Seasonal variations of photochemical tracers at low and middle latitudes on Mars: observations and models. *Icarus* 201 (2), 564–569.
- Krasnopolsky, V.A., Lefevre, F., et al., 2013. Chemistry of the atmospheres of Mars, Venus, and Titan. In: Mackwell, S.J., et al. (Eds.), *Comparative Climatology of Terrestrial Planets*. Univ. of Arizona, Tucson, pp. 231–275. https://doi.org/10.2458/azu_uapress_9780816530595-ch11.
- Lane, A.L., Barth, C.A., Hord, C.W., Stewart, A.I., 1973. Mariner 9 ultraviolet spectrometer: observations of ozone on Mars. *Icarus* 18, 102–108.
- Lebonnois, S., et al., 2006. Vertical distribution of ozone on Mars as measured by SPICAM/Mars Express using stellar occultations. *J. Geophys. Res.* 111, E09S06.
- Lehmann, R., 2004. An algorithm for the determination of all significant pathways in chemical reaction systems. *J. Atmos. Chem.* 47, 45–78.
- Lefevre, F., Lebonnois, S., Montmessin, F., Forget, F., 2004. Three-dimensional modeling of ozone on Mars. *J. Geophys. Res.* 109, E07004.
- Lefevre, F., et al., 2008. Heterogeneous chemistry in the atmosphere of Mars. *Nature* 454, 971–975.
- Lewis, S.R., Collins, M., Read, P.L., Forget, F., Hourdin, F., Fournier, R., Hourdin, C., Talagrand, O., Huot, J.P., 1999. A climate database for Mars. *J. Geophys. Res.* 104, 24177–24194.
- Maltagliati, L., Montmessin, F., Fedorova, A., Korabiev, O., Forget, F., Bertaux, J.-L., 2011. Evidence of water vapor in excess of saturation in the atmosphere of Mars. *Science* 333, 1868–1871.
- Maltagliati, L., Montmessin, F., Korabiev, O., Fedorova, A., Forget, F., Määttänen, A., Lefevre, F., Bertaux, J.-L., 2013. Annual survey of water vapor vertical distribution and water–aerosol coupling in the martian atmosphere observed by SPICAM/MEX solar occultations. *Icarus* 223 (2), 942–962.
- McElroy, M.B., Donahue, T.M., 1972. Stability of the Martian atmosphere. *Science* 177, 986–988.
- Millour, E., Forget, F., Spiga, A., Navarro, T., Madeleine, J.-B., Montabone, L., Pottier, A., Lefevre, F., Montmessin, F., Chaufray, J.-Y., Lopez-Valverde, M.A., 2015. The Mars climate database (MCD version 5.2). In: *European Planetary Science Congress 2015*.
- Montmessin, F., Lefevre, F., 2013. Transport-driven formation of a polar ozone layer on Mars. *Nat. Geosci.* 6, 930–933. <https://doi.org/10.1038/ngeo1957>.
- Moreau, D., Esposito, L.W., Brasseur, G., 1991. The chemical composition of the dust-free Martian atmosphere: preliminary results of a two-dimensional model. *J. Geophys. Res.* 96 (B5), 7933–7945. <https://doi.org/10.1029/90JB02544>.
- Moudden, Y., McConnell, J.C., 2005. A new model for multiscale modeling of the Martian atmosphere, GM3. *J. Geophys. Res.* 110, E04001. <https://doi.org/10.1029/2004JE002354>.
- Moudden, Y., 2007. Simulated seasonal variations of hydrogen peroxide in the atmosphere of Mars. *Planet Space Sci.* 55, 2137–2143.
- Moudden, Y., McConnell, J.C., 2007. Three-dimensional on-line chemical modeling in a Mars general circulation model. *Icarus* 188, 18–34.
- Nair, H., Allen, M., Anbar, A.D., Yung, Y.L., Clancy, T., 1994. A photochemical model of the Martian atmosphere. *Icarus* 111, 124–150.
- Novak, R.E., Mumma, M.J., DiSanti, M.A., Dello Russo, N., 2002. Mapping of ozone and water in the atmosphere of Mars near the 1997 aphelion. *Icarus* 158, 14–23.
- Perrier, S., et al., 2006. Global distribution of total ozone on Mars from SPICAM/MEX UV measurements. *J. Geophys. Res.* 111, E09S06.
- Read, P.L., Collins, M., Forget, F., Fournier, R., Hourdin, F., Lewis, S.R., Talagrand, O., Taylor, F.W., Thomas, N.P.J., 1997. A GCM climate database for Mars: for mission planning and for scientific studies. *Adv. Space Res.* 19, 1213–1222.
- Richardson, M.I., Wilson, R.J., 2002. Investigation of the nature and stability of the Martian seasonal water cycle with a general circulation model. *J. Geophys. Res.* 107, E55031.
- Shaposhnikov, D.S., Rodin, A.V., Medvedev, A.S., 2016. The water cycle in the general circulation model of the Martian atmosphere. *Solar Syst. Res.* 50 (2), 90–101.
- Shimazaki, T., Shimizu, M., 1979. The seasonal variation of ozone density in the Martian atmosphere. *J. Geophys. Res.* 84 (A4), 1269–1276.
- Shimazaki, T., 1981. A model of temporal variations in ozone density in the Martian atmosphere. *Planet. Space Sci.* 29 (1), 21–33. ISSN 0032-0633.
- Smith, M.D., 2002. The annual cycle of water vapor on Mars as observed by the Thermal Emission Spectrometer. *J. Geophys. Res.* 107 (E11), 5115.
- Smith, M.D., Wolff, M.J., Clancy, R.T., Murchie, S.L., 2009. CRISM observations of water vapor and carbon monoxide. *J. Geophys. Res.* 114, E00D03.
- Steele, L., Balme, M.R., Lewis, S.R., Spiga, A., 2017. The water cycle and regolith–atmosphere interaction at Gale crater, Mars. *Icarus* 289, 56–79.
- Stock, J.W., Blaszcak-Boxe, C.S., Grenfell, J.L., Lehmann, R., Patzer, A.B.C., Rauer, H., Yung, Y.L., 2012. Chemical pathway analysis of the Martian atmosphere: CO₂-formation pathways. *Icarus* 219 (1), 13–24.
- Stock, J.W., Blaszcak-Boxe, C.S., Lehmann, R., Grenfell, J.L., Beate, A., Patzer, C., Rauer, H., Yung, Y.L., 2017. A detailed pathway analysis of the chemical reaction system generating the Martian vertical ozone profile. *Icarus* 291, 192–202. <https://doi.org/10.1016/j.icarus.2016.12.012>.
- Toigo, A., Smith, M.D., Seelos, F.P., Murchie, S.L., 2013. High spatial and temporal resolution sampling of Martian gas abundances from CRISM spectra. *J. Geophys. Res.* 118, 89–104.

- Trainer, M.G., et al., 2014. Seasonal variation of atmospheric mixing ratios on Mars measured by the MSL SAM instrument. In: 45th Lunar and Planetary Science Conference. Houston, USA.
- Traub, W.A., Carleton, N.P., Connes, P., Noxon, J.F., 1979. The latitude variation of O₂ dayglow and O₃ abundance on Mars. *Astrophys. J.* 229, 846–854.
- Wehrbein, W.M., Hord, C.W., Barth, C.A., 1979. Mariner 9 ultraviolet spectrometer experiment: vertical distribution of ozone on Mars. *Icarus* 38, 188–199.
- Willame, Y., Vandaele, A.C., Depiesse, C., Lefevre, F., Letocart, V., Gillotay, D., Montmessin, F., 2017. Retrieving cloud, dust and ozone abundances in the Martian atmosphere using SPICAM/UV nadir spectra. *Planet. Space Sci.* 142, 9–25.
- Wolff, et al., 2010. Ultraviolet dust aerosol properties as observed by MARCI. *Icarus* 208, 143–155.
- Yung, Y.L., DeMore, W.B., 1999. *Photochemistry of Planetary Atmospheres*. Oxford University Press, New York.
- Zhu, X., Yee, J.-H., Talaat, E.R., 2007. Effect of dynamical-photochemical coupling on oxygen airglow emission and implications for daytime ozone retrieved from 1.27 μ m emission. *J. Geophys. Res.* 112, D20304. <https://doi.org/10.1029/2007JD008447>.